UCRL-ID-119749

Recent Upgrades and Enhancements of the FEM3A Model

Stevens T. Chan

December 1994

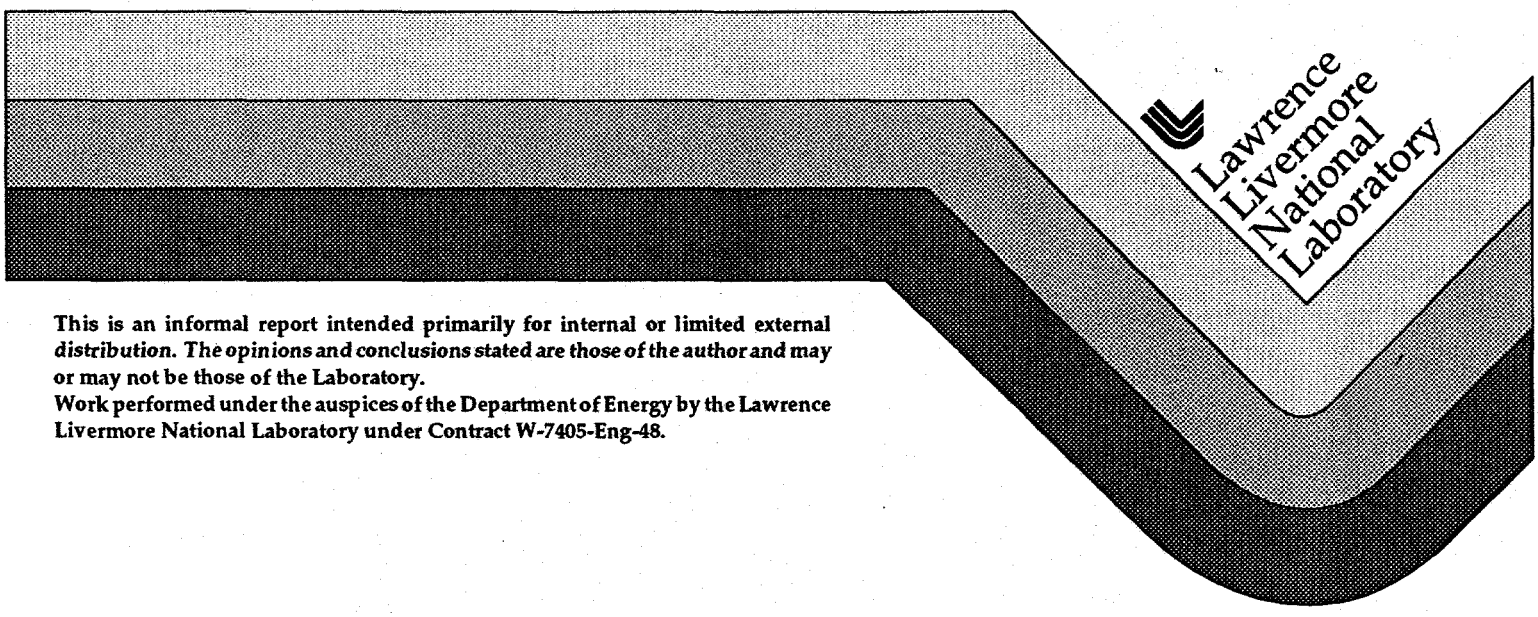

Work performed under the auspices of the Department of Energy by the Lawrence Livermore National Laboratory under Contract W-7405-Eng-48.

Recent Upgrades and Enhancements of the FEM3A Model

S.T. Chan
Lawrence Livermore National Laboratory

Summary

In 1984, the U.S. Army Edgewood Research, Development and Engineering Center began to fund Lawrence Livermore National Laboratory to further develop FEM3, a fully three-dimensional heavy-gas dispersion model, as a research tool for studying the atmospheric transport and diffusion of certain chemical systems. As a result, a significantly improved version of the model, called FEM3A, was delivered to ERDEC in 1988. During the past few years, two more major improvements have been developed and tested. They are: improved mass conservation for treating dispersion scenarios with large density variations, and the addition of an advanced turbulence submodel based on the $k-\epsilon$ transport equations. These enhancements have resulted in substantial improvements in the dispersion simulations of heavy-gases and can greatly extend the range of applicability of the model, including the ability to treat problems with large density variations and dispersion scenarios of much greater complexities. Documented in this report are the new features and some of the improvements obtained with the new model.

1. INTRODUCTION

During the early 1980s, Lawrence Livermore National Laboratory (LLNL) developed a three-dimensional finite element model called FEM3 (Chan, 1983) for simulating the atmospheric dispersion of liquefied natural gas (LNG) and other heavier-than-air gas (or heavy gas) releases. The model is based on solving, via a modified Galerkin finite element method, the set of time-dependent conservation equations of mass, momentum, energy, and species, together with the ideal gas law for the density of the gas/air mixture. A generalized anelastic formulation is used to preclude sound waves and to allow density variations to go beyond the range of the Boussinesq approximation (~0.3). Turbulence is modeled via an algebraic *K*-theory approach with certain ad hoc modifications to account for the presence of a heavy-gas cloud. The model can handle both continuous and finite duration releases, and terrain effects as well. Over the years, FEM3 has been validated to a large extent using data obtained from both laboratory-scale and field-scale heavy-gas dispersion experiments (see, for example, Ermak *et al.*, 1982; Chan *et al.*, 1984; Ermak and Chan, 1985; Havens *et al.*, 1987).

In 1984, the U.S. Army Edgewood Research, Development and Engineering Center (ERDEC, formerly known as U.S. Army Chemical Research, Development and Engineering Center) began to fund LLNL to further develop FEM3 as a research tool for studying the atmospheric transport and diffusion of certain chemical warfare systems. As a result, a newer version of the model, called FEM3A (Chan, 1988), was created and delivered to ERDEC in 1988. Besides being more user-friendly, FEM3A offers many new capabilities, including the treatment of multiple and overlapping sources, material phase-change, and the ability to handle obstructions such as buildings, dikes, and tanks. Additionally, an iterative solver for the pressure

equation was implemented to enable the code to solve problems of larger size, and with greater efficiency, than was previously feasible with a direct solver. Some of the applications and evaluation studies of FEM3A can be found in Ermak and Chan (1986), Rodean (1987a), Chan *et al.* (1987a), and Chan (1992).

During the past few years, two more major improvements have been developed to further extend the range of applicability of the FEM3A model. They are: improved mass conservation to treat dispersion scenarios with density variations much larger than the LNG range (~0.6), and the addition of an advanced turbulence submodel based on the $k-\varepsilon$ transport equations. In the first area, the source of deficiency with the original formulation has been identified and effective remedies, based on solving a slightly modified set of governing equations and an additional constraint for conserving global mass, have been developed and tested. The $k-\varepsilon$ turbulence submodel, owing to more complete physics, has resulted in substantially improved predictions for the dispersion simulations considered in this report and can greatly improve the code's ability in dealing with dispersion scenarios of greater complexities. User's guides for using the upgraded model, FEM3C, are documented in Chan (1994).

In the next section, the theoretical basis of the FEM3A model is first summarized to provide a basis for subsequent discussions. In section 3, the issues and remedies regarding mass conservation and the treatment of dispersion involving large density variations are discussed, with the effectiveness of the new algorithm demonstrated by numerical examples. In section 4, the formulation and implementation of the $k-\varepsilon$ turbulence submodel are described, together with numerical results to demonstrate the improvements obtained with this advanced turbulence submodel. Finally, some concluding remarks are given in the last section.

2. *THE FEM3A MODEL*

In this section, we describe briefly the theoretical basis of the FEM3A model. These include the governing equations, boundary conditions, initial conditions, and the submodels for representing the source, turbulence parameterization, ground heat transfer, and treatment of phase-change of the dispersed materials. More details of the model can be found in Chan (1988).

2.1 Governing Equations

The following three-dimensional, generalized anelastic equations, written for the mean (time-averaged) quantities in a turbulent flow field, are solved in FEM3A:

$$\frac{\partial(\rho \mathbf{u})}{\partial t} + \rho \mathbf{u} \cdot \nabla \mathbf{u} = -\nabla p + \nabla \cdot (\rho \mathbf{K}^m \cdot \nabla \mathbf{u}) + (\rho - \rho_h)\mathbf{g}, \tag{2.1}$$

$$\nabla \cdot (\rho \mathbf{u}) = 0, \tag{2.2}$$

$$\frac{\partial \theta}{\partial t} + \mathbf{u} \cdot \nabla \theta = \frac{1}{\rho C_p} \nabla \cdot (\rho C_p \mathbf{K}^\theta \cdot \nabla \theta) + \frac{C_{pv} - C_{pa}}{C_p} (K^c \cdot \nabla q_v) \cdot \nabla \theta + \frac{C_{pl} - C_{pa}}{C_p} (K^c \cdot \nabla q_l) \cdot \nabla \theta - \frac{L}{C_p} \left(\frac{\partial q_v}{\partial t} \right)_{pc}, \tag{2.3}$$

$$\frac{\partial q_v}{\partial t} + \mathbf{u} \cdot \nabla q_v = \frac{1}{\rho} \nabla \cdot (\rho K^c \cdot \nabla q_v) + \left(\frac{\partial q_v}{\partial t} \right)_{pc}, \tag{2.4}$$

$$\frac{\partial q_l}{\partial t} + \mathbf{u} \cdot \nabla q_l = \frac{1}{\rho} \nabla \cdot (\rho K^c \cdot \nabla q_l) - \left(\frac{\partial q_v}{\partial t} \right)_{pc}, \tag{2.5}$$

and

$$\rho = \frac{PM}{RT} = \frac{PM_a}{RT\left[1 + \left(\frac{M_a}{M_v} - 1\right) q_v - q_l\right]}. \tag{2.6}$$

In the above equations,

$\mathbf{u}$	=	velocity field = (u, v, w),
ρ	=	mixture density,
p	=	pressure deviation from a hydrostatic pressure field (p_h) corresponding to an adiabatic atmosphere (i.e., constant potential temperature) at rest,
ρ_h	=	density field corresponding to the adiabatic base state,
$\mathbf{g}$	=	acceleration due to gravity,
θ	=	potential temperature deviation from an adiabatic atmosphere at θ_0 (reference temperature),

q_v	=	mass fraction of material in vapor phase,
q_ℓ	=	mass fraction of material in liquid phase,
K^m, K^θ, K^c	=	eddy diffusion tensors for momentum, energy, and species, respectively,
C_{pa}	=	specific heat of the ambient atmosphere,
C_{pv}	=	specific heat of the dispersed material in vapor phase,
$C_{p\ell}$	=	specific heat of the liquid material,
C_p	=	specific heat of the mixture = $C_{pv}q_v + C_{p\ell}q_\ell + (1-q_v-q_\ell)C_{pa}$,
L	=	latent heat of phase-change for the dispersed material,
∇	=	gradient operator,
t	=	time,
$\left(\frac{\partial q_v}{\partial t}\right)_{pc}$	=	time rate of change of material vapor due to phase-change,
M	=	molecular weight of the mixture,
M_a	=	molecular weight of air,
M_v	=	molecular weight of the material in vapor phase,
P	=	total pressure = p_h + p,
R	=	universal gas constant,
T	=	absolute temperature = $(\theta+\theta_0)\left[(P/1000\ mb)^{R/MC_p}\right]$.

For problems of current interest, because the heights of interest are generally small (<<1 km), the ratio P/1000 mb is approximately equal to unity, hence no distinction is made between the absolute and potential temperature in the present model (which is fortunate since the above relationship is strictly valid only when R/MC_p is constant).

The above conservation equations were obtained by generalizing the anelastic approximation of Ogura and Phillips (1962). The essential features of the present generalized anelastic conservation equations are that variable density is allowed and sound waves are filtered a priori (thus time steps are not restricted by acoustic effects). The proper interpretation of neglecting $\partial\rho/\partial t$ in the total mass conservation equation is that acoustic density variations in time are assumed to be of very small amplitude and occur so quickly that it is a good approximation to assume density is always in (temporal) equilibrium with the other thermodynamic variables. The time dependence of density is then determined implicitly by the time variation of temperature, pressure, and composition via the ideal gas law. It is not appropriate to interpret equation (2.2) as implying $\partial\rho/\partial t = 0$, since ρ does indeed vary with time. More detailed discussions of the generalized anelastic formulation can be found in Lee *et al.* (1983).

The equations for energy and species, as seen above, contain no source terms other than that due to material phase-change. The source material and the associated temperature field are instead defined by either boundary conditions (to model an evaporating area source for continuous or finite-duration spills) or initial conditions (for instantaneous sources).

2.2 *Submodels*

Source characterizations

For continuous or finite-duration spills, the released source materials are modelled by vertically injecting the materials, which can be in both vapor and liquid phases, from a preselected area on the ground surface. Over such area, a constant mass flux $\dot{m}$ ($\dot{m} = \rho v$, v being the vertical velocity) is imposed for the duration of the spill.

In general, the total mass flux per unit area can be separated into

$$\dot{m}_v = \dot{m}F \tag{2.7a}$$

for material vapor and

$$\dot{m}_\ell = \dot{m}(1-F) \tag{2.7b}$$

for liquid material. In the above equation, F is the material fraction in vapor phase as determined by

$$F = C_{p\ell}(T_\ell - T_b)/L\ , \tag{2.8}$$

where

$C_{p\ell}$ = specific heat of liquid at constant pressure,

T_ℓ = liquid temperature,

T_b = boiling point of liquid at atmospheric pressure, and

L = latent heat of vaporization.

Equation (2.7) is implemented in the computer model as boundary conditions for the species equations in the following form,

$$K_v^c \frac{\partial q_v}{\partial n} = \dot{m}(F - q_v)/\rho \tag{2.9a}$$

and

$$K_v^c \frac{\partial q_\ell}{\partial n} = \dot{m}(1 - F - q_\ell)/\rho \tag{2.9b}$$

in which K_v^c is the eddy diffusivity in the vertical direction for the material species.

For the temperature equation, generalization of the enthalpy balance over the vapor source (see Ermak and Chan, 1985) leads to

$$K_v^\theta \frac{\partial \theta}{\partial n} = \dot{m}\left\{\left[C_{pv}F + C_{pl}(1-F)\right]\ \theta_l / C_p - \theta\right\} / \rho\ , \qquad (2.10)$$

in which the new symbols are defined as

K_v^θ = eddy diffusivity in the vertical direction for the energy equation, and

θ_l = liquid temperature measured from the reference temperature θ_0.

During source injection, the following boundary condition is also imposed over the source area for the vertical momentum equation,

$$\rho v = \dot{m}\ . \qquad (2.11)$$

After a finite-duration spill is terminated, the above boundary conditions are changed to correspond to zero fluxes ($\dot{m} = 0$) in Eqs. (2.9) through (2.11).

For instantaneous releases, a different source submodel is employed. For each instantaneous source, a group of mesh points within the computational domain is designated to represent the desired source configuration filled with the material to be released. In each source region, with the total mass fraction specified, appropriate initial values for vapor and liquid concentrations, together with the mixture temperature, are determined based on local thermodynamic equilibrium. In order to minimize the spatial oscillations in the concentration and temperature solutions due to the presence of short wave lengths (relative to the grid spacings) in the initial conditions, the initial concentration and temperature fields are often extended (smoothed) by trivariate Gaussian functions in the region immediately surrounding the nodes representing the sources. Within each source region, velocity is set equal to zero and hydrostatic pressure is assumed prior to release of the source material. Upon initialization of the release, these constraints are removed to simulate the instantaneous release of the sources. The FEM3A model is capable of treating multiple and overlapping instantaneous sources. More details and numerical examples can be found in Chan (1988).

Turbulence Parameterization

In FEM3A, turbulence is parameterized using a K-theory local equilibrium model. The turbulence diffusion tensors $\mathbf{K}^m$, $\mathbf{K}^\theta$, $\mathbf{K}^c$ are assumed to be diagonal and it is further assumed that $\mathbf{K}^\theta = \mathbf{K}^c$. Specifically, the vertical diffusion coefficient (for all transport equations) is given by

$$K_v = \frac{k\left[(u_{a*})^2 + (w_*)^2\right]^{1/2} z}{\Phi}\ , \qquad (2.12)$$

where

k = von Karman's constant = 0.4,

u_{a*} = friction velocity of the ambient atmosphere,

z = height above ground surface,

w_* = in-cloud "convection velocity" = $0.5\left[(g/T)v_g(T_{gr}-T)z\right]^{1/3}$, in which g is the constant of gravitational acceleration, T is the cloud temperature, T_{gr} is the ambient ground temperature, and v_g is the effective heat transfer velocity between the ground and the vapor cloud, and

Φ = Monin-Obukhov profile function.

The form of the Monin-Obukhov profile function, Φ, is taken from Dyer (1974). When the Richardson number (see Eq. (2.14) below) is greater or equal to zero, Φ is defined as

$$\Phi = 1 + 5\ \mathrm{Ri}, \qquad \mathrm{Ri} \geq 0 \tag{2.13a}$$

for all three (momentum, energy, and species) vertical diffusion coefficients. When the Richardson number is less than zero, Φ is defined as

$$\Phi = \begin{cases} (1-16\ \mathrm{Ri})^{-1/4} & \text{for momentum,} \\ (1-16\ \mathrm{Ri})^{-1/2} & \text{for energy and species.} \end{cases} \qquad Ri < 0 \tag{2.13b}$$

The local Richardson number is, in turn, defined by an *ad hoc* approach of "combining" the turbulence in the ambient atmosphere and the stabilizing density stratification effects of the dispersing species,

$$Ri = Ri_a \frac{u_{*e}^2}{\left(u_{*e}^2 + w_*^2\right)} + nk^2(z/h_c)^n \frac{(\rho - \rho_a)}{\rho} \frac{gz}{\left(u_{*e}^2 + w_*^2\right)} \tag{2.14}$$

where the new symbols are defined below:

Ri_a = Richardson number of the ambient atmosphere = z/L, L being the Monin-Obukhov length scale,

ρ_a = density of the ambient atmosphere,

n = 2, an empirical constant based on the experimental results of McQuaid (1976),

h_c = characteristic cloud height.

The first term on the right hand size of Eq. (2.14) is designed to include the turbulence in the ambient atmosphere and the second term represents the effects of density stratification, which is generally a reduction of turbulence in the stably stratified, dense gas cloud. As can be seen, for isothermal, neutrally buoyant gas or in the absence of a dispersing cloud, the present submodel recovers the ambient diffusivities. A typical Richardson number profile has a zero value at ground level and a maximum value near the top of the vapor cloud, where large-density gradient and small-shear stresses normally exist.

The horizontal diffusion coefficient, K_h, is expressed as

$$K_h = \alpha k u_{a*} z/\Phi_a \ , \qquad (2.15)$$

where $\Phi_a = \Phi(Ri_a)$ and α is an empirical parameter with a value of 6.5, which was inferred from the Pasquill-Gifford curves for the horizontal and vertical dispersion coefficients σ_y and σ_z.

Phase-change submodel

The present phase-change submodel is an extension of the humidity model developed by Leone *et al.* (1985) for a moist atmosphere to treat the phase transition between water vapor and droplets. It is based on the assumption of local thermodynamic equilibrium. Other physical processes such as rainout, drop-size dependence, and chemical reactions are not included. Basically, this submodel utilizes the local values of partial pressure of material vapor (P_V) via the ideal gas law, and the saturation vapor pressure (P_V*) via the Antoine equation, together with the inventory of the vapor and liquid materials, to determine the amount of material undergoing phase-transition. If too much vapor is present ($P_V > P_V*$), the excess vapor must be condensed; if too little vapor is present ($P_V < P_V*$), enough liquid material must be evaporated to restore equilibrium (of course, only as much liquid material as is present can be evaporated and this fact is incorporated). The phase-transition, however, is complicated by a feedback mechanism between the energy and the species equations. That is, when vapor condenses, latent heat is released, thus raising T and P_V* to suppress vapor condensation. On the other hand, when liquid evaporates, latent heat is absorbed, thus decreasing T and P_V* to prevent further evaporation of the liquid material. Therefore, these equations must be considered as a coupled system. The relevant numerical procedures are described in Chan (1988).

Ground Heat Transfer

For heavy-gas dispersion problems involving cryogenic materials, e.g., liquefied natural gas (LNG), the effects of heat transfer from the warmer ground surface into the colder vapor cloud could significantly affect the dispersion process. The main effects from such ground heating are the decrease in mixture density and the increase of turbulence intensity, both of which tend to enhance the mixing and dilution of the vapor cloud.

A bulk coefficient submodel is currently used for the energy equation to account for the heat flux from the ground surface, i.e.,

$$K_v^{\theta} \frac{\partial \theta}{\partial n} = v_E(\theta_{gr} - \theta) \ , \qquad (2.16)$$

where v_E is an effective energy transfer velocity obtained from field measurements, θ_{gr} is the ground temperature, and θ is the computed temperature on the lower boundary of the computational domain. For the Burro series of LNG spill experiments (Koopman, *et al.* 1982), the value of v_E was found to be approximately 0.0125 m/s.

2.3 Boundary Conditions

Figure 2.1 illustrates the typical boundary conditions used in a heavy-gas dispersion simulation. Note the orientation of the coordinate system and the corresponding velocity components being used, which were chosen for the convenience of handling both two- and three-dimensional problems in one code. The origin of the coordinate system is normally placed at the center of the source area (in the case of a continuous/finite-duration spill) and the mean wind is assumed to be parallel to the *x*-*y* plane.

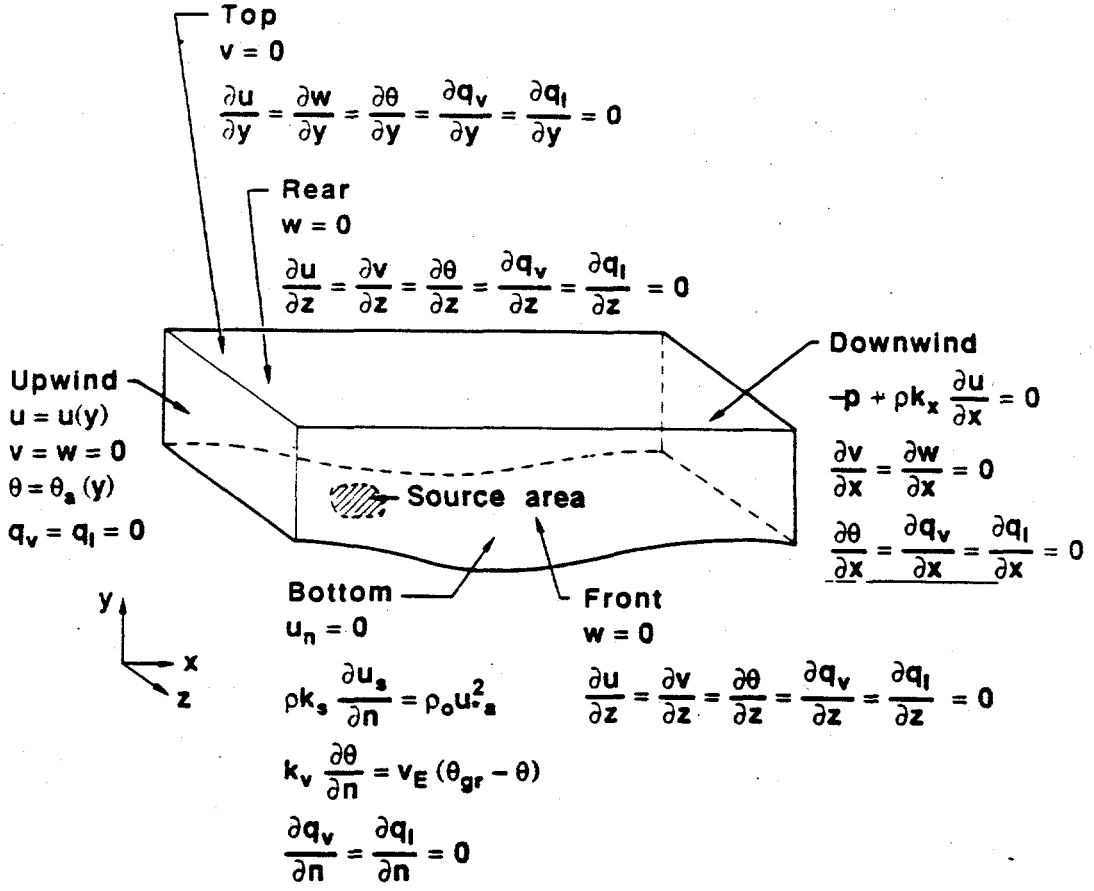

Fig. 2.1. Typical boundary conditions for the governing equations solved by the FEM3A model.

A wind profile is specified at the upwind boundary. This profile is expressed as a function of height above ground level. In nature it is usually a logarithmic profile with zero velocity on the ground surface. However, in practice, due to the use of coarse grids, a data-fitted parabolic or logarithmic profile, together with a "slip velocity" on the ground, is often used to better represent the overall ambient wind profile without attempting to resolve the surface "logarithmic sublayer." The remaining variables on this surface are normally specified to correspond to the ambient conditions. (Note: θ is the deviation temperature from the reference temperature, θ_o).

Natural boundary conditions, a by-product of the GFEM, are normally specified at the downwind (outflow) boundary. These conditions include zero normal "traction" for momentum in the x-direction and zero normal gradients for the remaining variables. On the top and lateral boundaries, which presumably are "far enough" from the vapor cloud, the respective normal velocity component and normal gradients of the remaining variables are set equal to zero.

On the ground surface excluding the source area, either no-slip (zero velocity) or generalized "partial slip" boundary conditions are specified for the momentum equations. No-slip boundary conditions are appropriate provided sufficiently fine grid spacings are used to resolve the surface sublayer; otherwise, the "partial slip" boundary conditions are more appropriate. In this case, the velocity component normal to the ground surface must be set equal to zero and shear stresses must be specified in the tangential directions. For the case involving variable terrain, appropriate local normal and tangential directions must be determined for the nodal points involved (Engleman *et al.*, 1982). Presently, one of the tangential directions is chosen to be parallel to the x-y plane and, in this direction, a shear stress of $\rho_O u_*^2$ is specified. Zero shear stress is specified along the other tangential direction because of the lack of field data in that direction (the associated shear stress is presumably small). The appropriate boundary conditions for mass fractions outside the source area are $\partial q_\nu / \partial n = \partial q_l / \partial n$ i.e., there is no loss or gain of species on the ground surface.

For flat terrain, because the solution is usually symmetric about the vertical center plane, only one-half of the domain has to be considered. In this case, symmetry boundary conditions, namely, the velocity component and the gradient of all other variables in the normal direction being zero, should be applied on the center plane.

For finite duration spills, the flux boundary conditions of Eqs. (2.9) through (2.11) are imposed over the source area until the simulated source injection is terminated, after which the corresponding fluxes are set equal to zero for each appropriate variable.

2.4 Initial Conditions

Before the start of a dispersion simulation, initial conditions corresponding to the ambient atmosphere must be provided. These initial conditions may, depending on the pre-existing temperature field, correspond to either an isothermal or a stratified atmospheric flow. Generating the ambient flow field generally requires that the model be run without the species equations for a sufficient length of time to establish a steady-state wind field within the computational domain, starting with an assumed wind field and appropriate boundary conditions. The resulting steady-state wind field and corresponding temperature field are then used as initial conditions in the dispersion simulation.

For instantaneous spills, the steady-state wind field should also account for the presence of the sources which are treated as obstructions via imposing the appropriate boundary conditions discussed earlier. For an all-vapor dispersion simulation, the initial mass fraction of vapor and the corresponding temperature must also be specified for each of the instantaneous sources. For a simulation involving vapor/liquid material, the initial total mass fraction of the dispersed material must be specified for each source, from which the model will determine the appropriate vapor/liquid fractions of the source material, together with a consistent temperature field based on a local thermodynamic equilibrium submodel.

For continuous or finite-duration releases, since the injection-like source submodel (via Eqs. (2.9) through (2.11)) is employed, initial conditions for the species equations are always set equal to zero. In general, the initial wind field should also account for any terrain effects. For problems involving flat terrain, however, a wind field having a vertical profile identical to that at the inlet plane is often a good approximation to the initial wind field required in the dispersion simulation.

3. *IMPROVEMENTS IN MASS CONSERVATION*

In the FEM3A model, since the original generalized equations were derived as an extension of the classical Boussinesq equations to stretch the density change to a larger value (up to 0.6 for LNG—the material considered at the time), ensuring mass conservation was not thought to be an issue—as it is not considered an issue in the Boussinesq equations. In the past, the model has indeed been observed to conserve mass reasonably well, when density changes were in the LNG range and adequate mesh resolution was used. However, certain past applications (Rodean, 1987b) revealed that the lack of conservation for species and global mass was quite significant and sometimes deleterious, when much larger density changes (e.g., chlorine or hydrogen cyanide) were involved.

In the following, the problem of mass conservation with the anelastic equations solved by FEM3A is identified and cost-effective remedies are discussed. Following a description of algorithm implementation, two numerical examples are presented to demonstrate the improvements obtained with the new algorithm.

3.1 Deficiency of the 'Old' Equations

The governing equations being solved in FEM3A were presented in section 2. For convenience of discussion, they are presented once again in the following:

$$\frac{\partial(\rho\mathbf{u})}{\partial t}+\rho\mathbf{u}\cdot\nabla\mathbf{u}=-\nabla p+\nabla\cdot\left(\rho\mathbf{K}^{m}\cdot\nabla\mathbf{u}\right)+(\rho-\rho_h)\mathbf{g}, \tag{3.1}$$

$$\nabla\cdot(\rho\mathbf{u})=0\ , \tag{3.2}$$

$$\frac{\partial\theta}{\partial t}+\mathbf{u}\cdot\nabla\theta=\frac{1}{\rho C_p}\nabla\cdot\left(\rho C_p\ \mathbf{K}^{\theta}\cdot\nabla\theta\right)+\frac{C_{pv}-C_{pa}}{C_p}\left(\mathbf{K}^{c}\cdot\nabla q_v\right)\cdot\nabla\theta$$
$$+\frac{C_{pl}-C_{pa}}{C_p}\left(\mathbf{K}^{c}\cdot\nabla q_l\right)\cdot\nabla\theta-\frac{L}{C_p}\left(\frac{\partial q_v}{\partial t}\right)_{pc}\ , \tag{3.3}$$

$$\frac{\partial q_v}{\partial t}+\mathbf{u}\cdot\nabla q_v=\frac{1}{\rho}\nabla\cdot\left(\rho\mathbf{K}^{c}\cdot\nabla q_v\right)+\left(\frac{\partial q_v}{\partial t}\right)_{pc}\ , \tag{3.4}$$

$$\frac{\partial q_l}{\partial t}+\mathbf{u}\cdot\nabla q_l=\frac{1}{\rho}\nabla\cdot\left(\rho\mathbf{K}^{c}\cdot\nabla q_l\right)-\left(\frac{\partial q_v}{\partial t}\right)_{pc}\ , \tag{3.5}$$

$$\rho=\frac{PM}{RT}=\frac{PM_a}{RT\left[1+\left(\frac{M_a}{M_v}-1\right)q_v-q_l\right]}, \tag{3.6}$$

and

$$C_p = C_{pv} q_v + C_{pl} q_l + (1 - q_v - q_l) C_{pa} \ . \tag{3.7}$$

As is well known, the true continuity equation for a single- or multi-component continuum system is

$$\frac{\partial \rho}{\partial t} + \nabla \cdot (\rho \mathbf{u}) = 0. \tag{3.8a}$$

Its equivalent global mass conservation equation is

$$\frac{d}{dt} \int_{\Omega} \rho dv + \int_{\Gamma} \rho \mathbf{u} \cdot \mathbf{n} \ da = 0, \tag{3.8b}$$

in which Ω is the domain (fixed in time), Γ is the boundary of Ω, $\mathbf{u}$ is the velocity and $\mathbf{n}$ is the outward-directed unit normal vector.

For the anelastic equations solved in FEM3A, the mass conservation equation (3.2) implies

$$\int_{\Gamma} \rho \mathbf{u} \cdot \mathbf{n} \ da = 0 \ , \tag{3.9}$$

i.e., no net mass flow is allowed to leave (or enter) the domain. This is the only global conservation law contained in the 'old' code. Equations (3.8b) and (3.9), if both are true, imply the following global mass conservation equation for the generalized anelastic model,

$$\frac{d}{dt} \int_{\Omega} \rho \ dv = 0 \ . \tag{3.10}$$

However, because the density field is defined by the ideal gas law of (3.6) for which P, M and T are all time-dependent, rather than being obtained from (3.8a), there is no guarantee that equation (3.10) is actually satisfied by the existing model, i.e. there appears to be an inconsistency in the governing equations.

For species (other than air), the FEM3A model solves basically the following

$$\frac{\partial \omega_i}{\partial t} + \mathbf{u} \cdot \nabla \omega_i = \frac{1}{\rho} \nabla \cdot (\rho \mathbf{K}^e \cdot \nabla \omega_i), \tag{3.11}$$

in which $\omega_i (i = 1, 2)$ is the mass fraction of species i. For simplicity and clarity, the term involving phase-change has been purposely omitted, because a two-step scheme is used to treat the phase-change process and the term is irrelevant to the following discussions. Additionally, we assume herein the problem has a closed domain.

To study the conservation properties of (3.11), we first rewrite it, using (3.2), as

$$\rho \frac{\partial \omega_i}{\partial t} + \nabla \cdot (\rho \mathbf{u} \omega_i) = \nabla \cdot (\rho \mathbf{K}^e \cdot \nabla \omega_i) \ . \tag{3.12}$$

Next, we integrate over the domain, employing the divergence theorem and the boundary conditions that $\mathbf{u}\cdot\mathbf{n}=0$ and $\mathbf{n}\cdot\nabla\omega_i=0$ to yield

$$\int_\Omega \rho\frac{\partial\omega_i}{\partial t}dv=0, \tag{3.13}$$

which is the species "conservation law" built into the current model.

To assess this result, let us recall the rigorous species conservation equation,

$$\frac{\partial(\rho\omega_i)}{\partial t}+\nabla\cdot(\rho\mathbf{u}\omega_i)=\nabla\cdot(\rho\mathbf{K}^e\cdot\nabla\omega_i)\ . \tag{3.14}$$

Applying the same procedures used above, we obtain from (3.14) the following (rigorous) global species conservation equation,

$$\frac{d}{dt}\int_\Omega \rho\omega_i\ dv=0 \tag{3.15a}$$

or, equivalently,

$$\int_\Omega \rho\frac{\partial\omega_i}{\partial t}\ dv+\int_\Omega \omega_i\frac{\partial\rho}{\partial t}\ dv=0. \tag{3.15b}$$

In the current model, equation (3.15b) is generally not satisfied, although the first term is zero as a result of (3.13), but the second term is not. This is so, since $\omega_i>0$ *and* $\partial\rho/\partial t\neq 0$ because ρ varies owing to (3.6) and the fact that P, M, and T are time-dependent. If, for example, $\partial\rho/\partial t$ is largely negative in a region with high concentration of ω_i, the system will very likely lose "species i" as well as the total mass of all species. This probably explains the numerical results reported by Rodean (1987b), in which significant species mass was lost for instantaneous releases with high density variations.

3.2 Proposed Remedies

As discussed above, there are two aspects concerning the properties of mass conservation in the FEM3A model: (a) global conservation of individual species, and (b) global mass conservation of the mixture. Since the global conservation of individual species is important and since it also affects the global mass conservation of the mixture, we first discuss the remedy for species conservation.

As demonstrated above, solving (3.14) instead of (3.12) should ensure the desired property of global species conservation. Note, however, that equation (3.14) can be simplified, making use of (3.2), to yield

$$\frac{\partial(\rho\omega_i)}{\partial t}+\rho\mathbf{u}\cdot\nabla\omega_i=\nabla\cdot(\rho\mathbf{K}^e\cdot\nabla\omega_i)\ . \tag{3.16}$$

The above equation is preferred, because it is consistent with the momentum equations and is simpler to compute as well. Thus the first fix is to replace (3.11) with (3.16). If no phase-change is taking place, only one equation for species, i.e., $\omega_i = q_v$, has to be solved.

For problems involving phase-change, in order to conserve the contaminant in both vapor and liquid phases, equations (3.4) and (3.5) should be replaced by:

$$\frac{\partial(\rho q_v)}{\partial t} + \rho \mathbf{u} \cdot \nabla q_v = \nabla \cdot \left(\rho \mathbf{K}^c \cdot \nabla q_v\right) + \left[\frac{\partial(\rho q_v)}{\partial t}\right]_{pc}, \tag{3.4a}$$

and

$$\frac{\partial(\rho q_\ell)}{\partial t} + \rho \mathbf{u} \cdot \nabla q_\ell = \nabla \cdot \left(\rho \mathbf{K}^c \cdot \nabla q_\ell\right) - \left[\frac{\partial(\rho q_v)}{\partial t}\right]_{pc}. \tag{3.5a}$$

In addition, the last term of (3.3) should be replaced by

$$\frac{1}{\rho c_p}\left[\frac{\partial(\rho q_v)}{\partial t}\right]_{pc}.$$

It is to be noted that, since equation (3.14) (or its equivalent, 3.16) applies for every species except air, summation of (3.14) over all species including air does not lead to $\partial\rho/\partial t = 0$ because the conservation equation for air is not in the form of (3.14). An equation for air *can* be obtained by subtracting the summation of (3.14) over all species from (3.2) to yield

$$\frac{\partial(\rho\omega_a - \rho)}{\partial t} + \nabla \cdot (\rho \mathbf{u}\omega_a) = \nabla \cdot \left(\rho \mathbf{K}^c \cdot \nabla \omega_a\right). \tag{3.17}$$

in which $\omega_a \equiv$ the mass fraction of air $\equiv 1 - \sum^{N} \omega_i$. The presence of the spurious term $-\partial\rho/\partial t$ in equation (3.17) is a consequence of the generalized anelastic *approximation* (i.e., it is a consequence of the omission of $\partial\rho/\partial t$ in the mass conservation equation for the mixture). Such an error hopefully is not a concern with heavy-gas dispersion problems, for which the conservation of species is generally more important. Note too that by virtue of the global mass conservation equation, (3.10), the error is totally eliminated from a *global* conservation point of view.

We now address the remaining problem: conservation of total mass (and air mass). As derived earlier, equation (3.10) is the global mass conservation equation desired for the generalized anelastic model. Alternatively, the requirement can be stated as

$$\int_\Omega \rho \, dv = m^o, \tag{3.18}$$

in which m^o is the initial mass contained in the domain. Because the mixture density is defined by the ideal gas law and it is, in general, a function of the species composition, temperature, and pressure, equation (3.18) obviously will not hold under the most general circumstances

However, based on the premise that most of the density variations are caused by differences in molecular weight, species composition, and temperature, but not pressure, we propose to satisfy the equation by finding a pressure increment (δp) , which is spatially uniform but time-dependent, such that equation (3.18) *is* always true, i.e.,

$$\int_{\Omega} \frac{(P+\delta p)M}{RT} dv = m^{o} \quad . \tag{3.19}$$

From the above equation, the required pressure increment can be determined via

$$\delta p = \left(m_{O} - \int_{\Omega} \frac{PM}{RT} dv \right) \Big/ \int_{\Omega} \frac{M}{RT} dv. \tag{3.20}$$

After obtaining δp, the density field is updated to satisfy (3.19). The success and cost-effectiveness of the proposed remedy requires that $|\delta p / P| << 1$, so that resolving the discretized pressure Poisson equation is not necessary. This is usually the case, because the value of total pressure (including hydrostatic pressure) for most atmospheric problems is several orders of magnitude larger than δp.

The above approach has been tested and appeared to work satisfactorily for "contained" flows as will be demonstrated in our examples. For similar ideas in this direction, and different equations, see Chenoweth and Paolucci (1986).

3.3 Algorithm Implementation

In order to accommodate various kinds of heavy-gas dispersion scenarios, two mass-conservation options have been implemented and tested. They are:

A. Option to conserve species mass,
B. Option to conserve both species mass and global mass.

The first option is suitable for problems whose global mass is not known or inconvenient to determine, such as those with open boundaries and/or an area source; the second option is suitable for any problems whose global mass is known and remains constant in time.

Option A - Conserving Species Mass Only

With this option (and the next option too), the equations of species being solved are either (3.16) for contaminant in vapor only, or (3.4a) and (3.5a) for contaminant in vapor and liquid phases. In either case, the values of density for the individual species: $\rho_v (= \rho q_v)$ and $\rho_\ell (= \rho q_\ell)$, are computed directly, in a way similar to solving the momentum equations for the values of mass flux ρu, ρv, and ρw. After the values of species density (ρ_v, ρ_ℓ) are obtained, however, it is important to compute the resulting mixture density (ρ) and mass fractions (q_v, q_ℓ) in a consistent manner. An early approach using the following approximations (n is the time step number)

$$q_v^n = \rho_v^n / \rho^{n-1} ,$$

and

$$q_l^n = \rho_l^n / \rho^{n-1}$$

in (3.6) to evaluate the mixture density and then use it in the subsequent time-integration of the species equations has proven to be numerically unstable. For consistency, the following equation, instead of (3.6), is used to evaluate the mixture density

$$\rho^n = \frac{P^n M_a}{RT^n} - \left(\frac{M_a}{M_v} - 1\right)\rho_v^n + \rho_l^n \tag{3.21}$$

in which P^n is the total pressure at time step n. The corresponding values of mass fraction are then given consistently by

$$q_v^n = \rho_v^n / \rho^n , \tag{3.22a}$$

and

$$q_l^n = \rho_l^n / \rho^n . \tag{3.22b}$$

The entire numerical algorithm for this option is then basically the same as that to be described for option B (below) except removing step 7 from the time-marching process. For brevity, these procedures are omitted for this case.

Option B - Conserving Both Species Mass and Global Mass

This option is basically the previous one plus the constraint of (3.19). It is applicable only to problems for which the value of global mass is known *and* remains constant in time. In the following, we summarize first the matrix equations and then the relevant numerical procedures of the entire algorithm.

When the standard Galerkin finite element method is applied to equations (3.1), (3.2), (3.3), (3.4a) and (3.5a), the following coupled system of matrix equations is obtained:

$$M\dot{U} + [K + N(U)]u + CP = F, \tag{3.23}$$

$$C^T U = 0 , \tag{3.24}$$

$$M_S\dot{\theta} + [K_\theta + N_S(U)]\theta = F_\theta , \tag{3.25}$$

$$M_S\dot{\rho}_v + [K_v + N_S(U)]q_v = F_v , \tag{3.26}$$

and

$$M_S\dot{\rho}_\ell + [K_\ell + N_S(U)]q_\ell = F_\ell \ , \tag{3.27}$$

where U and u are global 3n vectors containing all nodal values of $\rho\mathbf{u}$ and $\mathbf{u}$, respectively, P is a global m-vector containing pressure values, M, K, and N (all 3n x 3n) are the mass matrix, the diffusion matrix, and the advection matrix, respectively, C is the 3n x m pressure gradient matrix, its transpose, C^T, is the m x 3n divergence matrix, and F is a 3n global vector incorporating natural boundary conditions (tractions) and the buoyancy force. The matrices for temperature (θ) and the density and mass fractions of material vapor (ρ_v, q_v) and liquid material (ρ_ℓ, q_ℓ) are defined similarly, except their "size" is n instead of 3n.

Equations (3.23) through (3.27) are integrated in time via a modified forward Euler method; that is, the physical diffusion tensors are augmented with a balancing diffusion tensor to compensate for the negative diffusion caused by the simple forward Euler method when applied to the advection term. Also, several cost-effective techniques, including mass lumping, reduced quadrature, subcycling and others, were implemented in the present model. These techniques were described in greater length by Gresho *et al.* (1984). Solution of the above system of equations can be divided basically into two parts, i.e., problem initialization and time marching.

The initialization process consists of essentially the following steps:

1. Compute the hydrostatic pressure field for a selected base-state (such as one with a constant reference temperature) and the density field, including contributions from all species.

2. With a given initial velocity field and the above density field, form a momentum field and project it onto a divergence-free subspace to satisfy equation (3.24).

3. Compute the initial (dynamic) pressure field corresponding to the above momentum field.

4. Update the density field to include contributions from the initial pressure.

5. Evaluate species density and the inventory of both initial species mass and global mass.

With the system properly initialized, the time-marching part, described below for $t = n\ \Delta t$, is composed of the following steps:

1. Form the partial acceleration vector (without the pressure gradient),

$$A^n = M^{-1}\left[F^n - Ku^n - N\left(U^n\right)u^n\right] .$$

2. Solve the linear algebraic system (discretized Poisson equation) for the dynamic pressure and update total pressure $\left(P^n\right)$,

$$\left(C^T M^{-1} C\right)p^n = C^T A^n \ , \text{ and}$$

$$P^n = P_h + p^n \ .$$

3. Update the mass flux, accounting for the pressure gradient,

$$U^{n+1} = U^n + \Delta t\left(A^n - M^{-1}Cp^n\right) .$$

4. Update the temperature and species density of the dispersed material,

$$\theta^{n+1} = \theta^n + \Delta t M_s^{-1}\left[F_\theta^n - K_\theta\,\theta^n - N_s\left(U^n\right)\theta^n\right] ,$$

$$\rho_v^{n+1} = \rho_v^n + \Delta t\, M_s^{-1}\left[F_v^n - K_v q_v^n - N_s\left(U^n\right)q_v^n\right] ,$$

and

$$\rho_\ell^{n+1} = \rho_\ell^n + \Delta t M_s^{-1}\left[F_\ell^n - K_\ell\, q_\ell^n - N_S\left(U^n\right)q_\ell^n\right] .$$

5. Update the density of mixture,

$$\rho^{n+1} = \frac{P^n M_a}{RT^{n+1}} - \left(\frac{M_a}{M_v} - 1\right)\rho_v^{n+1} + \rho_\ell^{n+1} . \tag{3.28}$$

6. Evaluate the inventory of global mass,

$$m^{n+1} = \int \rho^{n+1} dv = M_S\ \rho^{n+1} . \tag{3.29}$$

7. Determine pressure increment necessary in order to conserve global mass using equation (3.20),

$$\delta p = \left(m^O - m^{n+1}\right)\Big/ M_S\left(\rho^{n+1}/P^n\right) . \tag{3.30}$$

This step usually requires a few relatively inexpensive iterations involving equations (3.28) to (3.30), because the update of ρ^{n+1} to include δp affects the global mass m^{n+1}.

8. Invoke the phase-change submodel to adjust the values of species density.

9. Advance the time step and repeat steps 1 through 8.

3.4 Numerical Examples

In the following, two numerical examples are presented to illustrate the degree of discrepancies that resulted from the mass conserving and mass non-conserving schemes. The first example, with a maximum density ratio of 10, is used to demonstrate the importance of mass conservation; the second example, involving only moderate density changes, serves to vindicate the original formulation under such conditions. For both problems, the new algorithms require virtually the same computer time as the old algorithm.

3.4.1 A Heavy-Gas Source Instantaneously Released in a 3D Enclosure

In this example, a ground level source of heavy-gas material is instantaneously released and dispersed in a 3D enclosure of size 60 m × 60 m × 20 m (length × width × height). The released material is assumed to have a molecular weight 10 times that of air and the initial distribution of the source material is Gaussian about the source center on the ground surface with 100% mass fraction at the center. The standard deviations (sigma values) are 2 m in the vertical and 6 m in the horizontal directions, respectively. The source material is, therefore, contained in a dome, for which the contours of the density field on two representative planes are depicted in Fig. 3.1. For simplicity, the problem was assumed to be isothermal at T = 20°C and a vertical plane of symmetry was invoked to permit modeling only one-half of the problem domain.

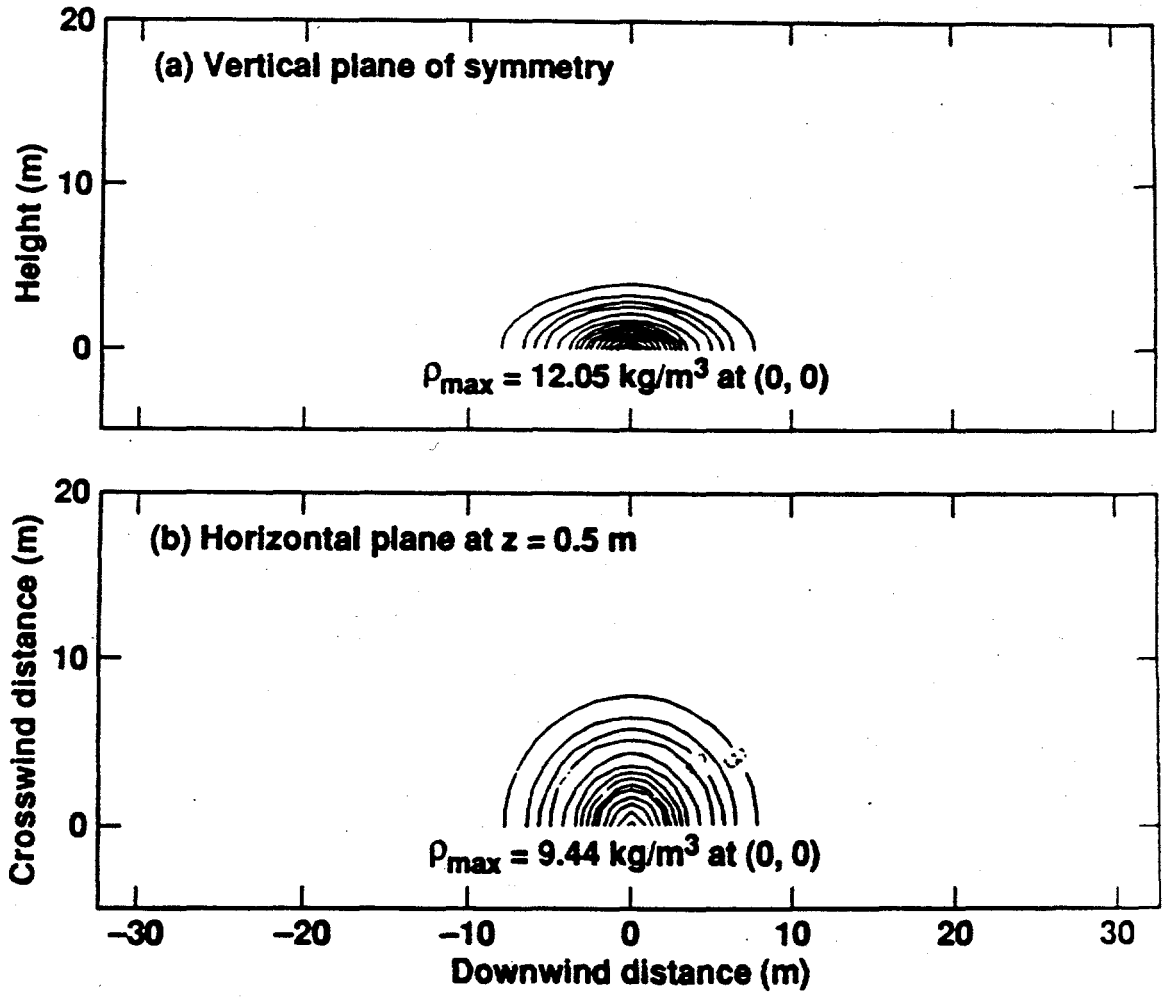

Fig. 3.1 Initial density contours on two representative planes. The contour levels are (in kg/m^3): B = 1.4, C = 1.6, D = 1.8, E = 2.0, F = 2.5, G = 3.0. H = 3.5, I = 4.0, J = 4.5, K = 5. L = 6, M = 7, N = 8, O = 9, P = 10, Q = 11, and R = 12.

With the origin of the coordinate system placed at the center of the source, the computational domain is defined by the following dimensions: -30 to 30 m longitudinally, 0 to 30 m laterally, and 0 to 20 m vertically. A graded mesh consisting of 5,952 mesh points (31 × 16 × 12 in the above three directions) was used. Additionally, constant diffusivities of 0.1 m^2/s in the vertical and 0.5 m^2/s in the horizontal directions were used. The problem was simulated for 10 s with a time step size of 0.05 s. No-slip conditions were used on all surfaces except the vertical plane of symmetry, wherein no penetration and zero tangential stresses were specified. For the contaminant, zero flux was imposed on the entire boundary.

The problem was solved via three different ways: the original (mass non-conserving) algorithm, the species-conserving scheme, and the scheme conserving both species and global mass. Since the velocity and concentration fields obtained with the two new schemes are hardly discernible graphically, we compare in the subsequent figures only those results obtained with the original and the species-conserving schemes. In Fig. 3.2, the time variations of the total inventory of species mass and global mass are compared. These results show that, at the end of the simulation, the original scheme has lost about 83 kg (~30%) in species mass and almost the same amount in global mass. On the other hand, the species-conserving scheme is not only able to conserve species mass exactly but is also able to conserve global mass reasonably well (but with some minor oscillations). The zig-zag behavior of the curves in Fig. 3.2(b) is due to the relaxation of the requirement of global mass conservation. It was indeed completely eliminated when the additional constraint (3.18) was imposed.

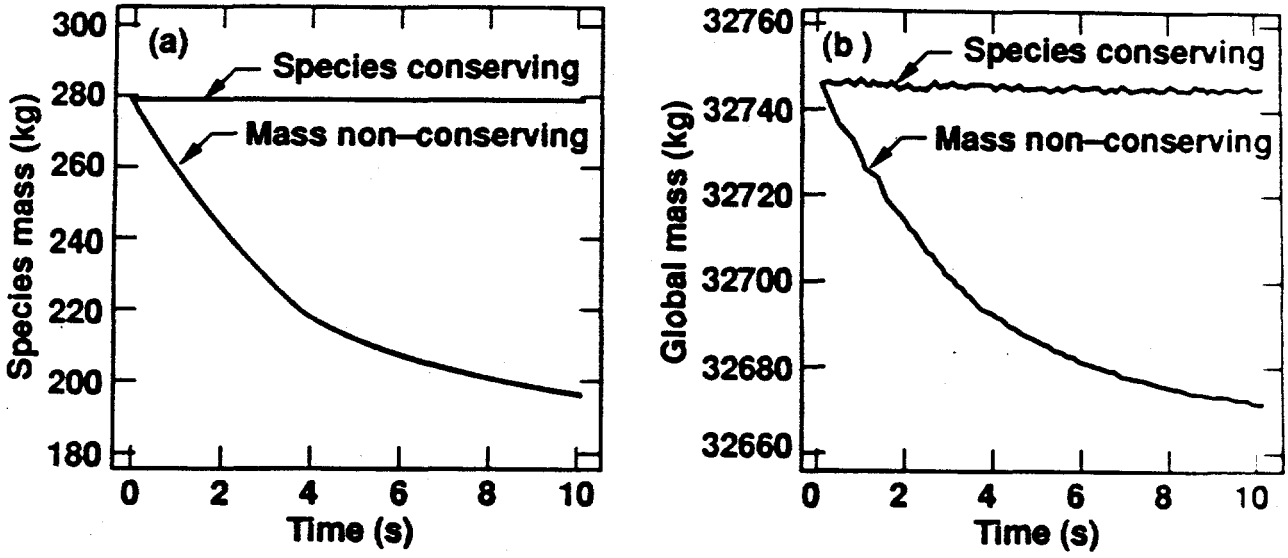

Fig. 3.2. Comparison of mass inventory for (a) species mass, and (b) global mass as obtained with the mass non-conserving and mass conserving schemes.

In Figs. 3.3 and 3.4, the concentration and velocity projection on two representative planes obtained with the two schemes are compared. These figures reveal a general agreement between the two numerical solutions regarding the overall flow field, the outward moving vortex ring, and the size of the vapor cloud. However, significant discrepancies also exist, especially in the region of higher concentration. For instance, the original scheme grossly under-predicts the maximum concentration and misses a couple of higher concentration contours. Also, the corresponding flow field is generally less energetic, with its maximum speed reduced by as much as 12%. Since the additional constraint of global mass conservation has practically no effects on the results, the errors associated with the original scheme are apparently due to the omission of the $\omega(\partial\rho/\partial t)$ term in the species conservation equation. Since the value of species concentration is always positive and the time rate of change of density is negative in the region with higher density, the omission of such a term is equivalent to adding a sink term in the species equation in such a region, wherein most of the species mass is contained. This explains why the original scheme suffers a substantial loss in species mass and global mass, as indicated in Fig. 3.2.

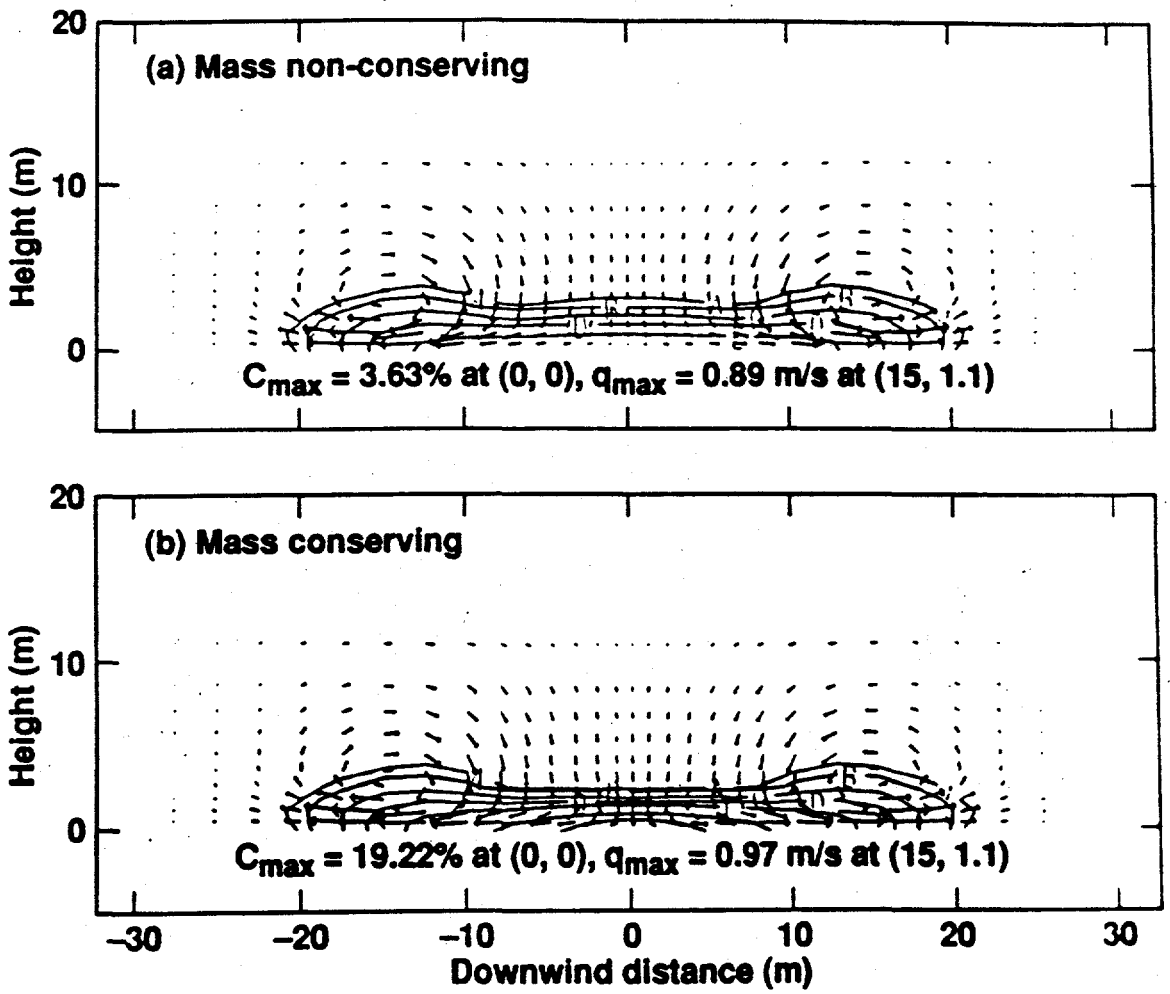

Fig. 3.3. Comparison of predicted concentration and velocity projection on the vertical plane of symmetry at time = 10 s with (a) mass non-conserving, and (b) mass conserving schemes. The contour levels are (in % vol): A = 0.1, B = 0.2, C = 0.5, D = 1, E = 2, F = 5, and G = 10.

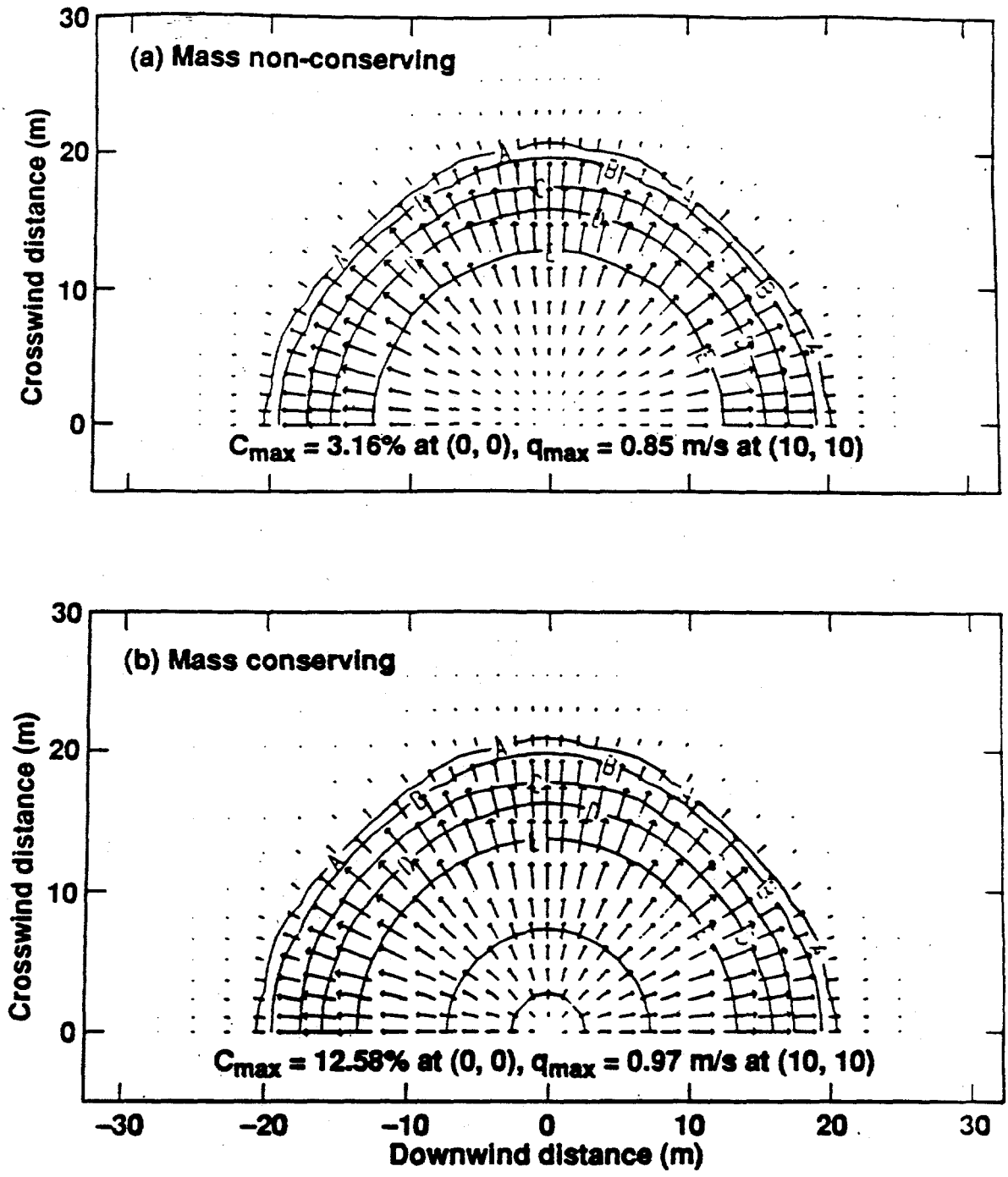

Fig. 3.4 Comparison of predicted concentration and velocity projection on the horizontal plane at z = 0.5 m and time = 10 s with (a) mass non-conserving, and (b) mass conserving schemes. The contour levels are (in % vol): A = 0.1, B = 0.2, C = 0.5, D = 1, E = 2, F = 5, and G = 10.

In Fig. 3.5, time history plots for two velocity components, density, and concentration at a selected location (6.5 m from the source center and 0.5 m above ground level) are compared. As is seen, the differences in velocity are quite noticeable; the discrepancies in density and concentration are even larger, with the difference in concentration by as much as a factor of two. These results clearly demonstrate the importance of mass conservation, especially species mass, in a problem involving large density changes.

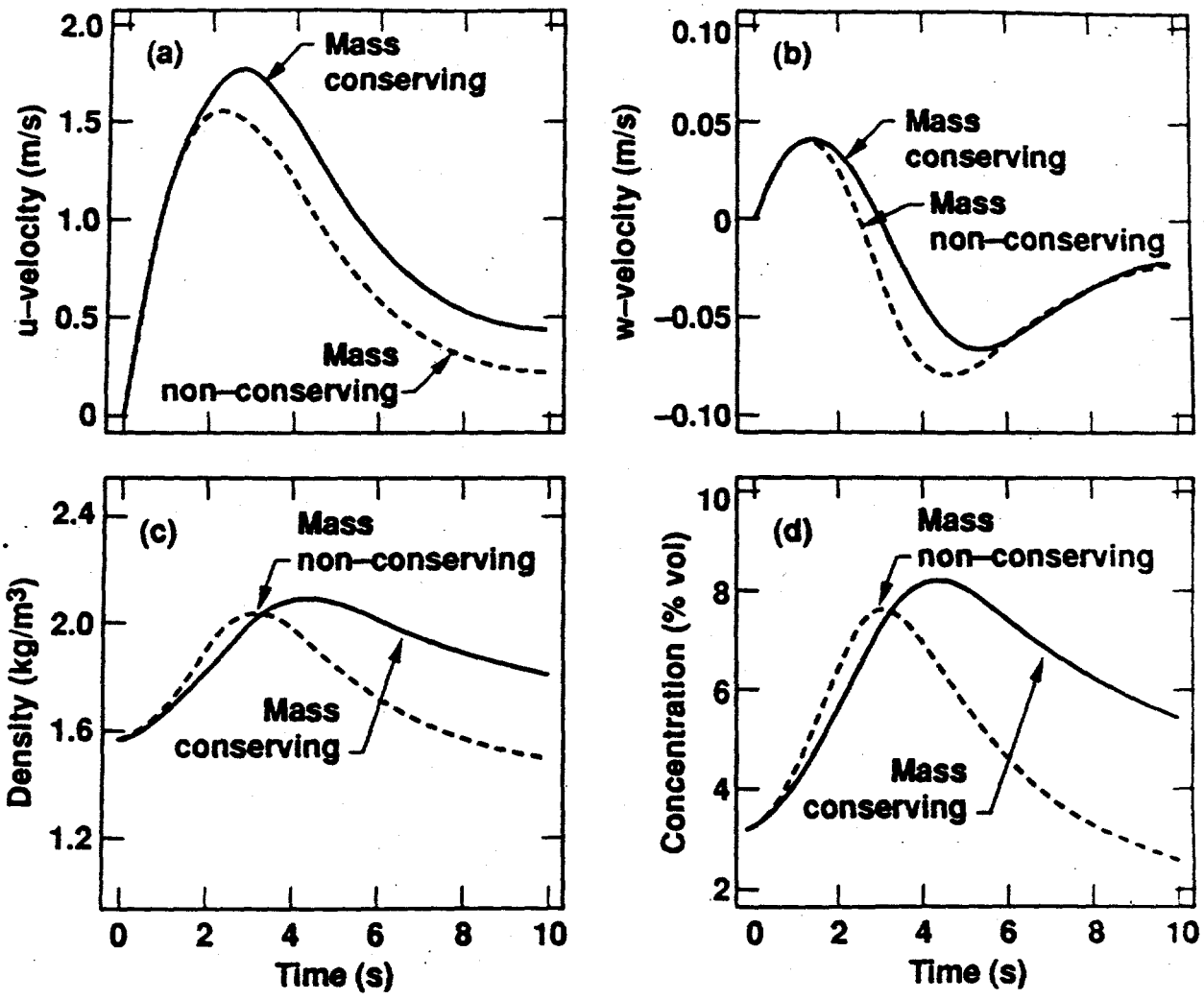

Fig. 3.5 Comparison of predicted field variables at 6.5 m from the source center and 0.5 m above the ground surface for (a) horizontal velocity, (b) vertical velocity, (c) density, and (d) concentration.

To evaluate the possible effects of temperature variations on the mass conservation properties, this problem was also simulated for a cold gas with the same initial concentration distribution. However, the molecular weight of the source material was reduced to 144.8 kg/kmole (five times that of air) and the mixture temperature was assumed to be Gaussian with a minimum value of 146.5 K (cf 293 K of the ambient air) at the source center so that the maximum mixture density remains at ten times that of the ambient air.

Results from the old and the new algorithms are, again, significantly different, especially in the source region. However, in spite of the noticeable differences in the inventory of global mass indicated in Fig. 3.6, results from the two new schemes are basically the same (~3 digits agreement) for all field variables.

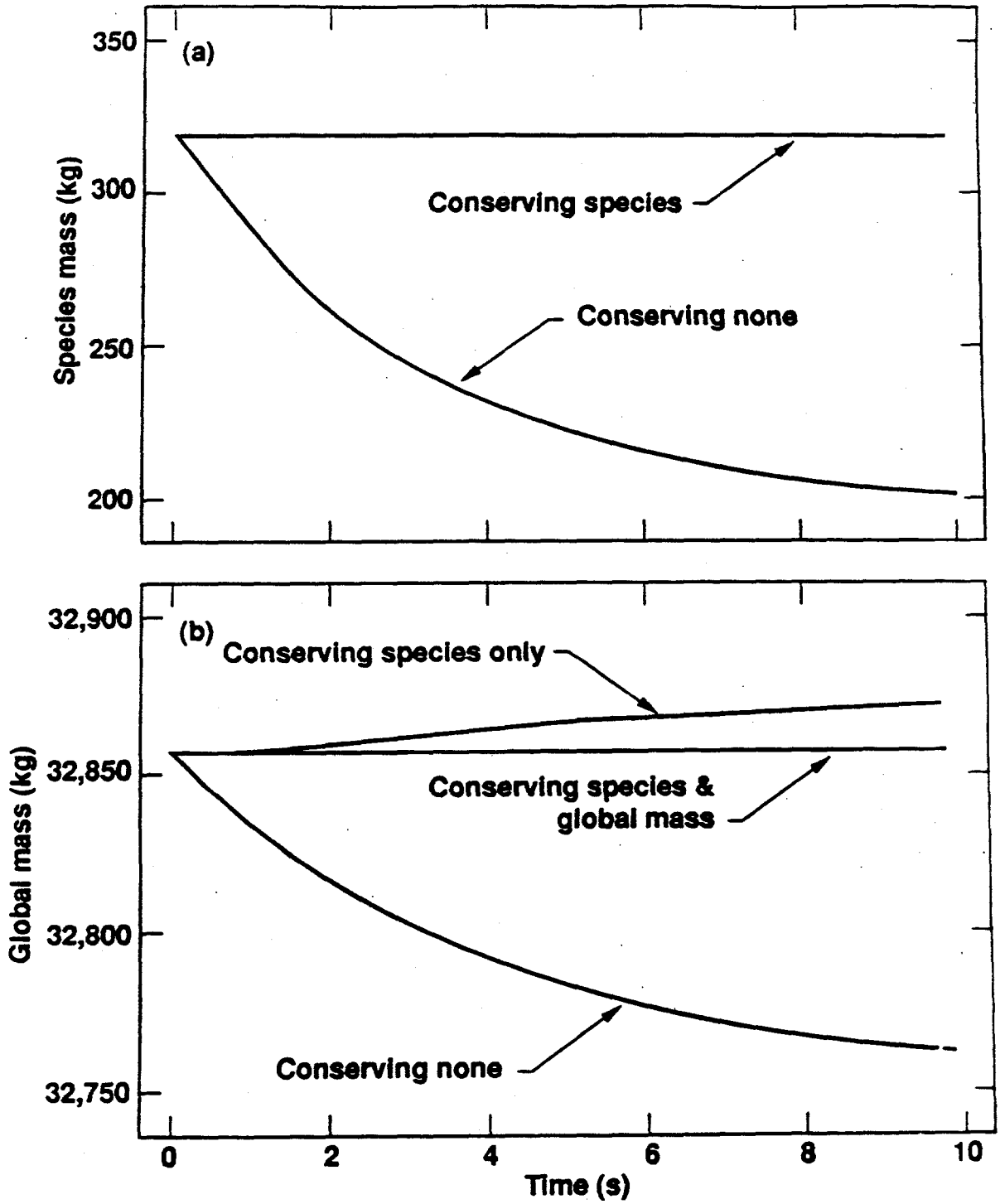

Fig. 3.6 Comparison of mass inventory for (a) species mass, and (b) global mass as obtained with the mass non-conserving and mass conserving schemes.

The slight overprediction in global mass by the species-conserving scheme, which can be attributed to the extra term of $\partial\rho/\partial t$ in equation (3.17), apparently has only minimal effects on the numerical solution. As the temperature field becomes more uniform towards the end of the simulation, the deviations in global mass starts to level off. In Fig. 3.7, contours of the density field on the horizontal plane at 0.5 m above ground as obtained with the old and the new algorithms are compared. Obviously, as the result of significant loss of species material in the source region (not shown), the density field predicted by the old algorithm is markedly lower.

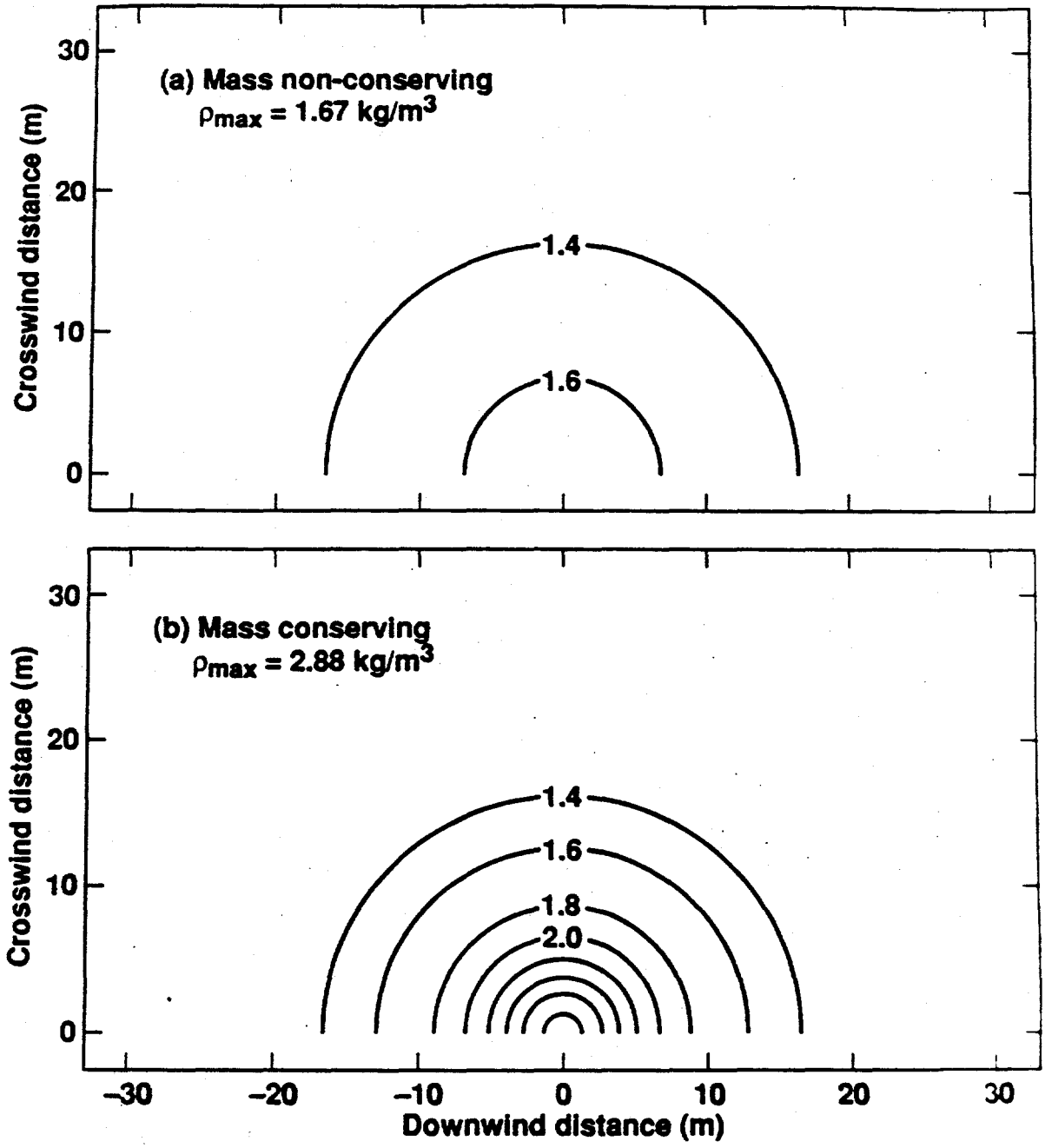

Fig. 3.7 Comparison of predicted density contours on the horizontal plane at z = 0.5 m and time = 10 s with (a) mass non-conserving and (b) mass conserving schemes.

3.4.2 Simulations of a HF Spill Experiment

As an example of practical applications, the formulations discussed above are used here to simulate a field experiment—the atmospheric dispersion of an aerosol cloud resulting from the pressurized release of liquid anhydrous hydrofluoric (HF) onto the ground. The particular test being simulated, test No. 1, is one of the six HF spill experiments jointly conducted by LLNL and Amoco Corp. at the U.S. Department of Energy Nevada Test Site during the summer of 1986 (Blewitt, *et al.*, 1987). This test was conducted under neutrally-stable atmospheric conditions, with an average wind speed of 5.6 m/s at the 2-m elevation. The ambient temperature was 37°C and the liquid HF temperature was 40 °C. A total of 4 m^3 liquid HF was released for a duration of 125 s, through a flashing jet from the end of a horizontal pipe pointed downwind. A preliminary simulation of the test was performed by Chan, *et al.* (1987b).

In the present simulation, the spill and ambient conditions have been changed slightly, based on the more up-to-date data (which are, unfortunately, relatively sparse) published by Blewitt, *et al.* (1987). Also a mesh with finer grid resolution near the ground was utilized. Due to the lack of a jet model, the source was approximated as an area source of 20 m × 20 m, with an injection velocity of 0.1 m/s. The friction velocity used in the *K*-theory turbulence submodel is 0.34 m/s and no heat transfer between the ground surface and the vapor cloud was assumed. It must be emphasized that, because of the sparsity of experimental data and the use of a relatively simple submodel to approximate the actual, complex source (in particular the jetting effects and aerosol generation), no serious attempt was made for a detailed model-data comparison. Rather, the main purpose here is to invoke the modified phase-change submodel and compare results from the old and the new algorithms.

In order to conserve computation time, lateral symmetry is assumed and thus only one-half of the vapor cloud is simulated. The computational domain has a height of 20 m, a lateral dimension of 60 m (for one-half of the cloud), and a longitudinal dimension extending from 20 m upwind of the spill point to 400 m downwind. A graded mesh consisting of 7,605 grid points ($15 \times 13 \times 39$) was used.

Owing to complications arising from non-zero mass flux over the source area and the presence of open boundaries, there is really no convenient way in imposing the constraint of global mass conservation. Therefore this problem was simulated only with the original and the species-conserving formulations. Based on the results obtained in the first example, relaxing the requirement of global mass conservation is, nevertheless, not expected to have too much adverse effects on the present solution, as long as species mass is accurately conserved. Listed in Table 1 are the total mass of HF in vapor and liquid phases for different times as obtained with the two formulations.

Table 1. Comparison of total amount of HF obtained with present and original formulations

Time (s)	(1) Present form (kg)	(2) Original form (kg)	(3) (2)-(1)	(4) $\frac{(3)}{(1)}$ 100%
10	140.82	146.41	5.59	3.97
20	282.69	288.42	5.73	2.03
30	424.55	429.46	4.91	1.16
40	566.41	570.06	3.65	0.64
50	708.07	710.18	2.11	0.30
60	847.37	847.51	0.14	0.02
70	975.32	972.31	-3.01	-0.31
80	1,076.19	1,068.23	-7.96	-0.74
90	1,140.63	1,127.14	-13.49	-1.18
100	1,172.81	1,155.23	-17.58	-1.50
110	1,182.15	1,162.67	-19.48	-1.65
120	1,179.19	1,159.62	-19.57	-1.66

As seen in this table, the total amount of HF obtained from the species-conserving scheme is essentially linear in time prior to t = 60 s, after which the time rate of change begins to decline because some of the dispersed material starts to leave the computational domain. Results from the two formulations are only a couple of percent different. Such differences are typical for the other field variables as well. The close agreement between the two numerical solutions is apparently attributable to the much smaller density variations in the present case. For example, the value of maximum mixture density is only about 50% higher than that of the ambient air and the region with 10% or higher density is largely confined within an area of 40 m × 10 m.

The fact that the original formulation produced slightly more species mass than desired initially but less HF material for subsequent times can probably be explained, again, by the missing term in the original species conservation equations (for both the vapor and liquid droplets). During early times, because of the continuous influx of cold HF material, the value of mixture density in the source region is increasing in time (as opposed to decreasing in time in the first example), the omission of the term is equivalent to the addition of a source term in the species equations. For times after t = 60 s, because more HF material is leaving the computational domain than coming in over the source area (as suggested by results from the species-conserving formulation), the density field is probably decreasing in time, thus creating in effect a sink term for the species equations (and thus the loss of species mass). Finally, as the solution approaches steady-state (as does the density field), the effect of the above missing term gradually diminishes and thus the loss of species mass begins to stabilize, as suggested by the results near the end of the simulation.

Due to the closeness of the two numerical solutions, we will present only certain sample results obtained with the new formulation and briefly compare them with data, if available. In Fig. 3.8, the predicted HF concentration contours on the vertical plane of symmetry and the horizontal plane 1 m above the ground surface for t = 60 s are depicted. This figure shows a HF

cloud that is nearly 50 m wide and is hugging the ground (note the height has been scaled up by a factor of 2), even though the molecular weight of HF is only 20.01 (versus 28.96 for air). Such heavy-gas behavior is caused by the low temperature and aerosol effects, namely, the presence of HF droplets and the related evaporative cooling. A cold and ground-hugging cloud was indeed observed during the field experiment.

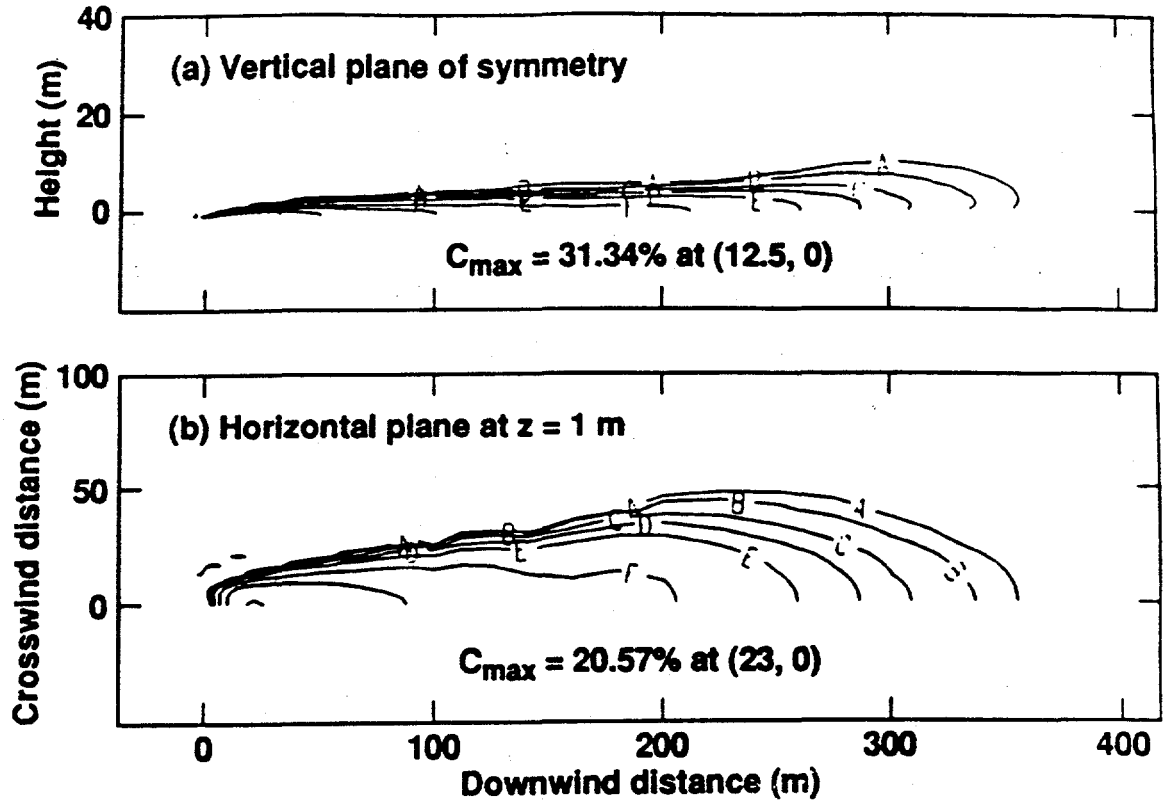

Fig. 3.8 Predicted HF concentration contours on two representative planes for Amoco HF spill test No. 1 at time = 60 s. The contour levels are (in % vol): A = 0.1, B = 0.2, C = 0.5, D = 1, E = 2, F = 5, G = 10, and H = 20.

In Fig. 3.9, the HF concentration contours on the crosswind plane at 300 m downwind are compared with measurements, which were reconstructed from Fig. 4-3 of Blewitt, *et al.* (1987), with the assumption that the cloud center is at +15 m off the array centerline. The experimental contours beyond +30 m (of the original plot) are much less reliable, because measurements are available only at 1 m high. It is to be noted that the experimental contours above 8 m were obtained by extrapolation because measurements were made at 1, 3, and 8 m high only. Nevertheless, the measurements strongly suggest a ground-hugging cloud and the FEM3A model is indeed able to predict a similar cloud, although the predicted cloud is somewhat lower and has higher concentration near the ground.

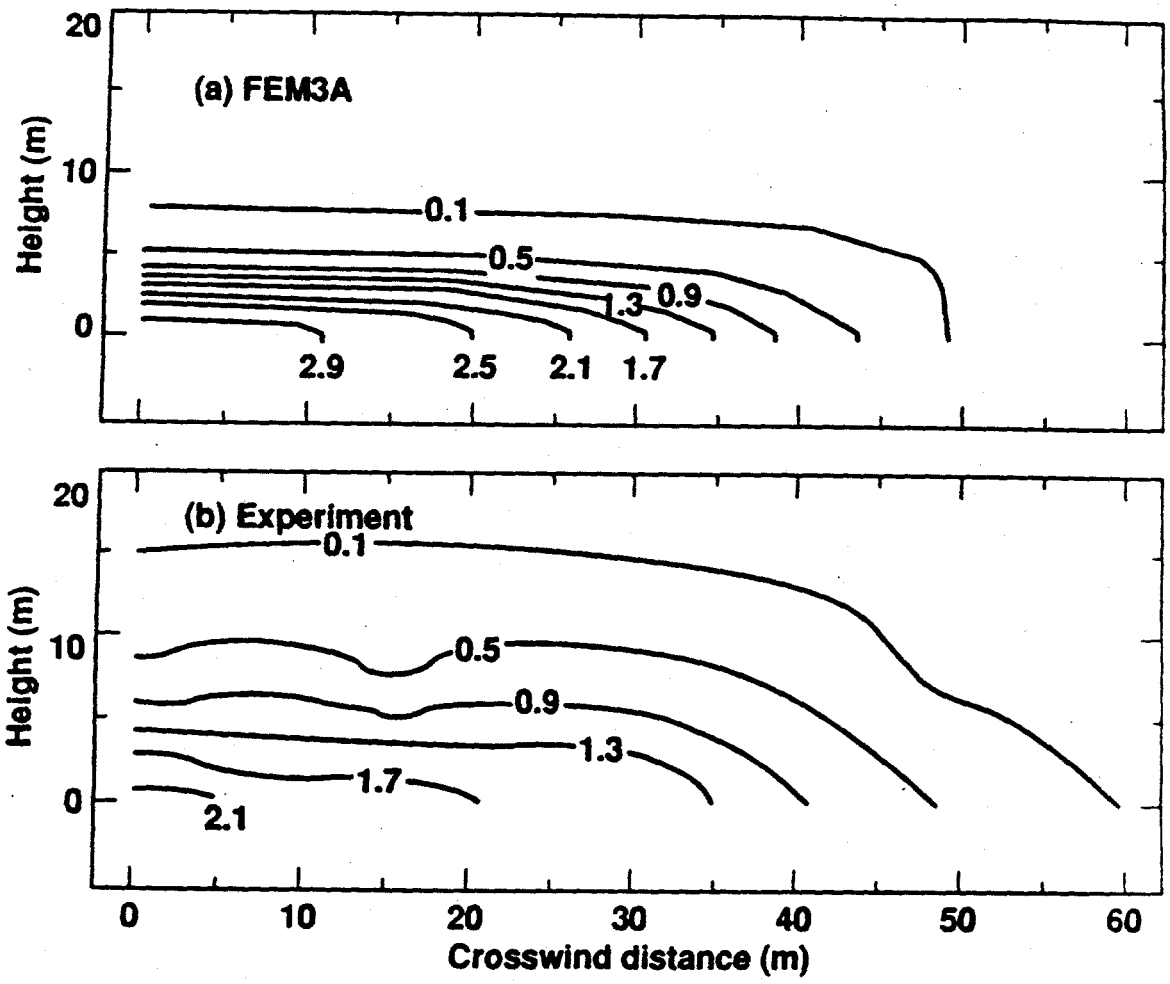

Fig. 3.9 Comparison of predicted versus measured concentration contours on the crosswind plane at 300 m downwind for Amoco HF spill test No. 1. The contour levels are in % vol. The FEM3A results are for time = 120 s and the measured data are for a 60 s averaging period beginning at time = 97.1s.

In Fig. 3.10, the predicted temperature along the cloud centerline at two different heights are displayed, together with the measured data (averaged over a 30-s period beginning at t = 121.3 s). Despite a greater difference in the source area, the overall agreement, regarding the general shape of the curves and the maximum change in temperature, is very good, especially at distances sufficiently far away from the source. The fact that warmer temperature was predicted in the source region is believed to be mainly due to the simplicity of the present source submodel, which neglects both the jetting effects and the cooling due to HF depolymerization (Schotte, 1987).

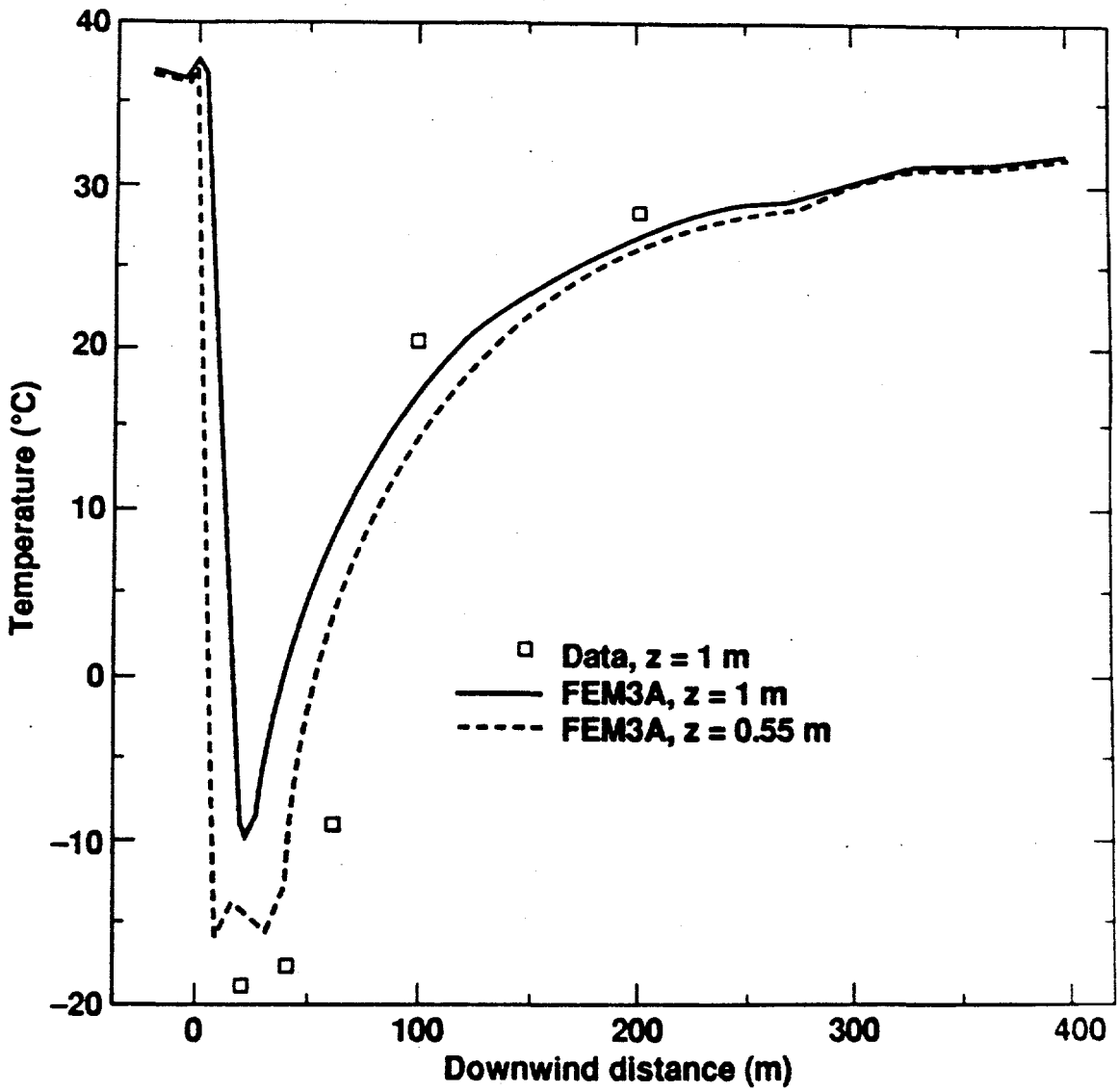

Fig. 3.10 Comparison of predicted versus measured temperature as a function of downwind distance for Amoco HF spill test No. 1. The FEM3A results are for time = 120 s and the measured data are for a 30 s averaging period beginning at time = 121.3 s

4. IMPROVED TURBULENCE MODELING

In the present section, further improvements to FEM3A in the area of turbulence modeling are described. Firstly the time-averaged flow equations based on the new generalized anelastic formulation are summarized. Turbulence modeling via a $k-\varepsilon$ formulation is then discussed. Numerical solution of the $k-\varepsilon$ equations and treatment of the various Reynolds stress terms are also described. Finally, two heavy-gas dispersion problems are presented to show the improvements obtained with the $k-\varepsilon$ model over the existing K-theory turbulence model.

4.1 The Time-Averaged Equations

As discussed in Section 3, the new model equations are (3.1), (3.2), (3.3), (3.4a), (3.5a), (3.6) and (3.7), with turbulent mixing modeled via the K-theory formulation described in Section 2. For convenience of describing the $k-\varepsilon$ turbulence model, these equations are recast in a Cartesian tensorial framework, together with the unknown turbulent fluxes such as $-\rho\overline{u_i'u_j'}$, $-\rho\overline{u_j'\theta'}$:

$$\frac{\partial}{\partial t}(\rho u_i)+\rho u_j\frac{\partial u_i}{\partial x_j}=-\frac{\partial p}{\partial x_i}+\frac{\partial}{\partial x_j}\left(-\rho\,\overline{u_i'u_j'}\right)+(\rho-\rho_h)\,g_i\ , \tag{4.1}$$

$$\frac{\partial}{\partial x_j}(\rho u_j)=0\ , \tag{4.2}$$

$$\frac{\partial\theta}{\partial t}+u_j\frac{\partial\theta}{\partial x_j}=\frac{1}{\rho C_p}\frac{\partial}{\partial x_j}\left(-C_p\,\rho\,\overline{u_j'\theta'}\right)+\frac{C_{pv}-C_{pa}}{\rho C_p}\left(-\rho\,\overline{u_j'q_v'}\right)\frac{\partial\theta}{\partial x_j}$$

$$+\frac{C_{p\ell}-C_{pa}}{\rho C_p}\left(-\rho\,\overline{u_j'q_\ell'}\right)\frac{\partial\theta}{\partial x_j}-\frac{L}{\rho\,C_p}\left[\frac{\partial}{\partial t}(\rho\,q_v)\right]_{pc}\ , \tag{4.3}$$

$$\frac{\partial}{\partial t}(\rho q_v)+\rho u_j\frac{\partial q_v}{\partial x_j}=\frac{\partial}{\partial x_j}\left(-\rho\,\overline{u_j'q_v'}\right)+\left[\frac{\partial}{\partial t}(\rho q_v)\right]_{pc}\ , \tag{4.4}$$

$$\frac{\partial}{\partial t}(\rho q_\ell)+\rho u_j\frac{\partial q_\ell}{\partial x_j}=\frac{\partial}{\partial x_j}\left(-\rho\overline{u_j'q_\ell'}\right)-\left[\frac{\partial}{\partial t}(\rho\,q_v)\right]_{pc}\ , \tag{4.5}$$

$$\rho=\frac{PM}{RT}=\frac{PM_a}{RT\left[1+\left(\dfrac{M_a}{M_v}-1\right)q_v-q_\ell\right]}\ , \tag{4.6}$$

and

$$C_p=C_{pv}q_v-C_{p\ell}q_\ell+(1-q_v-q_\ell)C_{pa}\ . \tag{4.7}$$

In the above equations, it has been assumed that turbulent density fluctuations produce only negligible dynamical effects in the mean transport equations, thus permitting the statistical correlations involving the fluctuating density component ρ' to be omitted. However, the dynamic effects resulting from mean density variations, in both space and time, are fully allowed for. As is seen, the above system of equations contain the unknown turbulent fluxes of momentum, energy, and mass fractions, which need to be approximated (or modeled) to arrive at a set of closed equations for the mean flow quantities. Described below is the $k-\varepsilon$ turbulence model implemented in the new computer code.

4.2 The $k-\varepsilon$ Turbulence Model

The isothermal version of the standard $k-\varepsilon$ turbulence model has been derived by Launder and Spalding (1974) and an extension to treat buoyancy was described by Rodi (1980). Based on these models, Haroutunian (1987) developed a new $k-\varepsilon$ turbulence model and applied it to simulate, with some success, the atmospheric dispersion of heavy gases. For the present model, we follow very much the lines of Haroutunian except that a simpler approach is taken for modeling anisotropic turbulence and the concept of flux Richardson number is employed to determine the turbulent Prandtl number.

In the standard $k-\varepsilon$ turbulence model, the unknown turbulence fluxes of momentum, energy, and mass fractions are approximated as:

$$-\rho\overline{u_i'u_j'} = \rho K\left(\frac{\partial u_i}{\partial x_j}+\frac{\partial u_j}{\partial x_i}\right)-\frac{2}{3}\rho\, k\,\delta_{ij}\ , \tag{4.8a}$$

$$-\rho\overline{u_i'\theta'} = \rho\frac{K}{Pr,\theta}\frac{\partial\theta}{\partial x_i}\ , \tag{4.8b}$$

$$-\rho\overline{u_i'q_v'} = \rho\frac{K}{Sc,c}\frac{\partial q_v}{\partial x_i}\ , \tag{4.8c}$$

$$-\rho\overline{u_i'q_\ell'} = \rho\frac{K}{Sc,c}\frac{\partial q_\ell}{\partial x_i}\ . \tag{4.8d}$$

In Eq. (4.8), K is the isotropic (or scalar) eddy viscosity, k is the turbulence kinetic energy, and Pr,θ and Sc,c are the turbulent Prandtl and Schmidt numbers. The eddy viscosity, in turn, is obtained from a Kolmogorov-Prandtl relationship of the form

$$K = C_\mu\ k^2/\varepsilon \tag{4.9}$$

in which

$$k = \frac{1}{2}\overline{u_i'u_i'} \tag{4.10a}$$

and

$$\varepsilon = \frac{\mu}{\rho}\,\overline{\frac{\partial u_i'}{\partial x_j}\,\frac{\partial u_i'}{\partial x_j}} \quad . \tag{4.10b}$$

In Eq. (4.9), C_μ is an empirical constant and ε is the viscous dissipation rate of turbulence kinetic energy.

The variables k and ε are governed by the following transport equations

$$\frac{\partial}{\partial t}(\rho k) + \rho u_j \frac{\partial k}{\partial x_j} = \frac{\partial}{\partial x_j}\left(\rho \frac{K}{\mathrm{Pr},k}\frac{\partial k}{\partial x_j}\right) + s + b - \rho\varepsilon \ , \tag{4.11}$$

$$\frac{\partial}{\partial t}(\rho\varepsilon) + \rho u_j \frac{\partial \varepsilon}{\partial x_j} = \frac{\partial}{\partial x_j}\left(\rho \frac{K}{\mathrm{Pr},\varepsilon}\frac{\partial \varepsilon}{\partial x_j}\right) + C_1\left(\frac{\varepsilon}{k}\right)s + C_1(1-C_3)\left(\frac{\varepsilon}{k}\right)b - C_2\,\rho\left(\frac{\varepsilon^2}{k}\right), \tag{4.12}$$

wherein Pr,k and Pr,ε are the turbulent Prandtl numbers for k and ε respectively. In Eq. (4.11), s is the production of turbulence kinetic energy resulting from interactions between the mean strain field and the turbulent stresses, and b is the production/destruction term resulting from the turbulent density fluctuations. The exact expressions for these two terms are

$$s = -\rho\,\overline{u_i' u_j'}\ \frac{\partial u_i}{\partial x_j} \tag{4.13a}$$

and

$$b = \overline{\rho' u_i'}\ g_i \ . \tag{4.13b}$$

These terms are modelled as

$$s = \rho K\left(\frac{\partial u_i}{\partial x_j} + \frac{\partial u_j}{\partial x_i}\right)\frac{\partial u_i}{\partial x_j} - \frac{2}{3}\rho k \frac{\partial u_k}{\partial x_k} \tag{4.14a}$$

and

$$b = -\frac{K}{Pr,\rho}\ \frac{\partial \rho}{\partial x_i}\, g_i \tag{4.14b}$$

in which Pr,ρ is the empirically prescribed turbulent Prandtl number for density.

In the ε equation, the modeling of the source/sink terms is largely based on intuition and dimensional reasoning, which is discussed in detail by Launder (1984). The terms $C_1(\varepsilon/k)s$ and $C_2\rho(\varepsilon^2/k)$ represent respectively the shear generation and viscous dissipation processes of ε, and C_1 and C_2 are model constants. The buoyancy term $C_1(1-C_3)(\varepsilon/k)b$ is also based on intuition and is due to Rodi (1980).

Values of the model constants used in the standard $k-\varepsilon$ model are:

$$C_\mu = 0.09, \quad C_1 = 1.44, \quad C_2 = 1.92, \quad Pr,k = 1.0, \quad Pr,\varepsilon = 1.3 \quad .$$

The remaining model coefficients, Pr,θ, Sc,c , Pr,ρ , and C_3 are flow dependent and need to be determined empirically. For simplicity and in the absence of relevant data to suggest the contrary, the above turbulent Prandtl/Schmidt numbers are assumed to be equal

$$Pr,\theta \;=\; Pr,\rho \;=\; Sc,c \;=\; Prt \tag{4.15}$$

wherein Prt is called the turbulent Prandtl number, which is a direct function of the local state of stratification and will be discussed shortly. The value of C_3 is rather controversial and should, in principle, be determined from "model tuning." For convenience, the values used by Betts and Haroutunian (1988), namely, -0.8 and 2.15 for the unstable and stable regions respectively are employed in the present study.

With the above standard $k-\varepsilon$ model, isotropic eddy viscosity/diffusivities are assumed. In order to model the turbulence process more appropriately for stratified flow such as heavy gas dispersion, the above $k-\varepsilon$ would have to be extended to allow for anisotropic turbulent diffusion. One such extension has been presented by Haroutunian (1987). The basic idea is to model the unknown turbulent fluxes with the following generalized *K*-theory expressions by replacing the scalar eddy viscosity/diffusivity with their corresponding eddy viscosity/diffusivity tensors. More specifically, Eq. (4.8) is rewritten as:

$$-\rho\,\overline{u_i' u_j'} = \rho\, K_{ijlm}\left(\frac{\partial u_l}{\partial x_m} + \frac{\partial u_m}{\partial x_l}\right) - \frac{2}{3}\rho k\,\delta_{ij} \quad , \tag{4.16a}$$

$$-\rho\,\overline{u_i'\theta'} = \rho K_{ij}^{\theta}\,\frac{\partial \theta}{\partial x_j} \quad , \tag{4.16b}$$

$$-\rho\,\overline{u_i' q_v'} = \rho K_{ij}^{c}\frac{\partial q_v}{\partial x_j} \quad , \tag{4.16c}$$

$$-\rho\,\overline{u_i' q_l'} = \rho K_{ij}^{c}\frac{\partial q_l}{\partial x_j} \quad . \tag{4.16d}$$

where K_{ijlm}, K_{ij}^{θ}, K_{ij}^{c} are the eddy viscosity/diffusivity tensors for momentum, energy, and mass fractions, respectively. K_{ijlm} is a fourth-order tensor, whereas K_{ij}^{θ} and K_{ij}^{c} are second-order tensors.

With the above concept and certain simplifying assumptions, a fairly sophisticated anisotropic turbulence model was derived by Haroutunian (1987) and used to simulate, among others, the dispersion of the dense gas cloud of the Burro 8 LNG (Liquefied Natural Gas) field trial conducted by Koopman, *et al.* (1982). Although the main features of the dense gas cloud were simulated reasonably well, the predicted vapor cloud was generally too low and too wide. Additionally, severe numerical difficulties were encountered when an attempt was made to include the actual terrain in the numerical simulation (Betts and Haroutunian, 1988) The

deficiencies of Haroutunian's model are probably due, in part, to the improper use of a geometry-dependent stratification parameter and wall-effect function in evaluating the turbulent Prandtl number, which is an important ingredient in modeling the turbulent fluxes of energy and mass fractions. Strictly speaking, the turbulent Prandtl number should be made a function of the flux Richardson number, which is defined by the buoyancy generation/destruction and the shear production terms in the turbulence kinetic energy equation.

In the present study, the flux Richardson number is employed. Additionally, in order to achieve a balance between model sophistication and computational cost, a simpler, ad-hoc approach to mimic the anisotropic turbulence diffusion in a dense gas cloud is adapted herein. Specifically, the anisotropic diffusion tensors are defined as:

$$K_{ijkm} \longrightarrow C_\mu \frac{k^2}{\varepsilon} \begin{Bmatrix} \beta_H & \beta_H & 1 \\ \beta_H & \beta_H & 1 \\ 1 & 1 & 1 \end{Bmatrix}, \tag{4.17a}$$

$$K_{ij}^{\theta} = K_{ij}^{c} = C_\mu \frac{k^2}{\varepsilon} \begin{bmatrix} \beta_H & 0 & 0 \\ 0 & \beta_H & 0 \\ 0 & 0 & 1 \end{bmatrix} \Big/ \mathrm{Pr}t \ , \tag{4.17b}$$

wherein β_H is an input (or tuning) parameter (usually greater than unity) of the model. Note that setting $\beta_H = 1$ leads to an isotropic diffusion model. Equation (4.17a) is a shorthand notation used to represent the nine non-zero elements of a fourth-order tensor and Eq. (4.17b) is a second-order tensor with non-zero entries for the diagonal terms only. The coordinate directions x, y, and z are assumed to be the principal directions, with $x-y$ on the horizontal plane and z being normal to the $x-y$ plane. Strictly speaking the value of β_H should depend on local stability conditions. However, for atmospheric boundary layer flow including heavy-gas dispersion problem, advection transport is usually dominating in the horizontal directions, its precise value is thus presumably not very crucial to the performance of the model. In the FEM3A model (Chan, 1988), a value of 6.5 was used in the K-theory turbulence model and appeared to perform reasonably well.

The turbulent fluxes and diffusivities for k and ε are defined in a similar way:

$$-\rho \overline{u_i' k'} = \rho K_{ij}^{k} \frac{\partial k}{\partial x_j} \ , \tag{4.18a}$$

$$-\rho \overline{u_i' \varepsilon'} = \rho K_{ij}^{\varepsilon} \frac{\partial \varepsilon}{\partial x_j} \ , \tag{4.18b}$$

with

$$K_{ij}^{k} = C_\mu \frac{k^2}{\varepsilon} \begin{bmatrix} \beta_H & 0 & 0 \\ 0 & \beta_H & 0 \\ 0 & 0 & 1 \end{bmatrix} \Big/ \mathrm{Pr},k \ , \tag{4.18c}$$

$$K_{ij}^{\varepsilon} = C_{\mu}\frac{k^2}{\varepsilon}\begin{bmatrix}\beta_H & 0 & 0\\ 0 & \beta_H & 0\\ 0 & 0 & 1\end{bmatrix}\Big/\mathrm{Pr},\varepsilon \quad . \tag{4.18d}$$

In the context of anisotropic turbulence diffusion, the shear production and buoyancy production/destruction of turbulent kinetic energy are modelled as

$$s = \rho\, K_{ijm}\left(\frac{\partial u_i}{\partial x_m}+\frac{\partial u_m}{\partial x_i}\right)\frac{\partial u_i}{\partial x_j} - \frac{2}{3}\rho\, k\frac{\partial u_i}{\partial x_i} \tag{4.19a}$$

and

$$b = -K_{ij}^{\rho}\frac{\partial \rho}{\partial x_j}g_i \quad , \tag{4.19b}$$

in which

$$K_{ij}^{\rho} = K_{ij}^{c} \quad . \tag{4.19c}$$

As alluded to earlier, the flux Richardson number, which is defined below, is more appropriate for determining the turbulent Prandtl number. Knowing the value of R_f,

$$R_f = -b/s \quad , \tag{4.20}$$

the inverse turbulent Prandtl number is then determined using the following relationship

$$\frac{1}{\mathrm{Pr}t} = \sigma_{to}\frac{\left(1-10R_f\right)}{\left(1-R_f\right)^2} \quad , \tag{4.21}$$

based on the fitting of certain atmospheric and laboratory data (Ueda *et al.*, 1981). In the present study, the value of σ_{to} is selected to be 0.9852 (instead of 1.2 used by Ueda *et al.*) based on the corrected similarity profiles (see Haroutunian, 1987) for the famous Kanas experiments. Also, in order to maintain realistic values for $\mathrm{Pr}t$, the range of R_f is set to be between -20 and 0.099.

4.3 Solution of the $k-\varepsilon$ Equations

With the $k-\varepsilon$ turbulence model, the governing equations being solved are (4.1) through (4.9), together with Eqs. (4.11) and (4.12) for the turbulence kinetic energy and its dissipation rate. The model is augmented by the turbulent Prandtl number defined by Eq. (4.21). For anisotropic turbulent mixing, a simple ad hoc approach described by Eqs. (4.16) through (4.19) is taken in the current study.

In the following, certain numerical aspects of the improved model are presented, which include a discussion of treating the turbulent flux terms in the momentum equation, a semi-implicit treatment of the sink terms in the k, ε equations, a clipping procedure designed to

eliminate the undesirable values of k and ε, and the associated boundary conditions. For convenience, the following discussion will be restricted to isotropic turbulence only; extension to include anisotropic turbulence is straightforward and, in principle, involves merely replacing the scalar diffusivities with their corresponding tensor diffusivities.

In order to retain a code structure that is useful for both the existing K-theory model and the new $k-\varepsilon$ turbulence model, the new terms arising from the $k-\varepsilon$ model in the momentum equations are treated as additional source/sink terms. As an illustration, the turbulent momentum flux term for the x-momentum equation is arranged in the following way,

$$
\begin{aligned}
-\frac{\partial}{\partial x_j}\left(\rho\overline{u'u'_j}\right) &= -\frac{\partial}{\partial x}\left(\rho\overline{u'u'}\right) - \frac{\partial}{\partial y}\left(\rho\overline{u'v'}\right) - \frac{\partial}{\partial z}\left(\rho\overline{u'w'}\right) \\
&= \frac{\partial}{\partial x}\left[\rho K\left(\frac{\partial u}{\partial x}+\frac{\partial u}{\partial x}\right)-\frac{2}{3}\rho k\right] \\
&\quad + \frac{\partial}{\partial y}\left[\rho K\left(\frac{\partial u}{\partial y}+\frac{\partial v}{\partial x}\right)\right]+\frac{\partial}{\partial z}\left[\rho K\left(\frac{\partial u}{\partial z}+\frac{\partial w}{\partial x}\right)\right] \\
&= \frac{\partial}{\partial x}\left(\rho K\frac{\partial u}{\partial x}\right)+\frac{\partial}{\partial y}\left(\rho K\frac{\partial u}{\partial y}\right)+\frac{\partial}{\partial z}\left(\rho K\frac{\partial u}{\partial z}\right)-\frac{\partial}{\partial x}\left(\frac{2}{3}\rho k\right) \\
&\quad + \frac{\partial}{\partial x}(\rho K)\frac{\partial u}{\partial x} + \frac{\partial}{\partial y}(\rho K)\frac{\partial v}{\partial x}+\frac{\partial}{\partial z}(\rho K)\frac{\partial w}{\partial x} \\
&\quad + \rho K\frac{\partial}{\partial x}\left(\frac{\partial u}{\partial x}+\frac{\partial v}{\partial y}+\frac{\partial w}{\partial z}\right).
\end{aligned}
$$

In the finite element formulation of the above terms, the first three terms are treated via the conventional Galerkin method of weighted residuals with integration by parts, thus yielding the same kind of natural boundary conditions as before. The fourth term is conveniently absorbed in the pressure gradient term, and the next three terms are treated as sources/sinks. The last term is assumed to be negligible (indeed, it vanishes for incompressible flow with constant density) and is thus omitted. The turbulent fluxes for other components of the momentum equation are treated in a similar manner.

Now, let us look at the numerical solution of the $k-\varepsilon$ Eqs., (4.11) and (4.12). These transport equations are similar to the species Eqs. (4.4) or (4.5) except the source/sink terms are different. Thus the finite element discretization procedures and time integration scheme described in the previous section still apply except special care must be taken of the viscous dissipation terms in these equations. Haroutunian (1987) observed that explicit treatment of the viscous dissipation terms, namely, $-\rho\varepsilon$ in the k equation and $-C_2\rho\left(\varepsilon^2/k\right)$ in the ε equation, are responsible for producing negative nodal values of k and ε, especially in regions of strong stable stratification, thus causing the numerical solution to diverge rapidly. As a means to stabilize the numerical algorithm, these terms are linearized and treated implicitly in time marching. Specifically, Eqs. (4.11) and (4.12) are rewritten as

$$
\frac{\partial}{\partial t}(\rho k)+\left(\frac{\rho\varepsilon}{\rho k}\right)(\rho k)+\rho u_j\frac{\partial k}{\partial x_j} = \frac{\partial}{\partial x_j}\left(\rho\frac{K}{\mathrm{Pr},k}\frac{\partial k}{\partial x_j}\right)+f_k\,, \tag{4.22}
$$

$$\frac{\partial}{\partial t}(\rho\varepsilon) + C_2\left(\frac{\rho\varepsilon}{\rho k}\right)(\rho\varepsilon) + \rho u_j \frac{\partial \varepsilon}{\partial x_j} = \frac{\partial}{\partial x_j}\left(\rho \frac{K}{\mathrm{Pr},\varepsilon} \frac{\partial \varepsilon}{\partial x_j}\right) + f_\varepsilon \ , \tag{4.23}$$

where

$$f_k = s + b \ ,$$
$$f_\varepsilon = C_1\left(\frac{\varepsilon}{k}\right)s + C_1(1-C_3)\left(\frac{\varepsilon}{k}\right)b \ .$$

Equations (4.22) and (4.23) are now in the same form and thus can be solved using the same numerical approach.

Summarized below are the procedures for obtaining the transient solution for the field of turbulence kinetic energy. After applying the Galerkin finite element method to Eq. (4.22), including integration by parts of the diffusion term, the following matrix equation is obtained:

$$M_s \frac{\partial}{\partial t}(\rho k) + a M_s (\rho k) + (K_k + N_s)\ k = F_k \tag{4.24}$$

where M_s, K_k, N_s are the mass matrix, the diffusion matrix, and the advection matrix respectively, F_k is a global vector incorporating natural boundary conditions and the source terms and "a" denotes the value of $\rho\varepsilon/\rho k$. For computational efficiency, a lumped (or diagonal) mass matrix, together with a vector containing the nodal values of "a", are used in the time integration scheme. By treating the second term of Eq. (4.24) implicitly and the remaining terms explicitly, one finally obtains the following time-stepping algorithm

$$(\rho k)^{n+1} = (\rho k)^n + \Delta t\, M_s^{-1}\left[F_k^n - (K_k + N_s)\ k^n\right]/(1 + \Delta t\, a^n) \tag{4.25}$$

with $a^n = (\rho\varepsilon)^n/(\rho k)^n$.

Similarly the time-stepping algorithm for $\rho\varepsilon$ is

$$(\rho\varepsilon)^{n+1} = (\rho\varepsilon)^n + \Delta t\, M_s^{-1}\left[F_\varepsilon^n - (K_\varepsilon + N_s)\varepsilon^n\right]/(1 + \Delta t\, b^n) \tag{4.26}$$

in which

$$b^n = C_2(\rho\varepsilon)^n/(\rho k)^n \ .$$

Once the nodal values of ρk and $\rho\varepsilon$ are obtained, the values of eddy viscosity at nodal points are evaluated according to

$$K = C_\mu(\rho k)^2/(\rho \cdot \rho\varepsilon) \ . \tag{4.27}$$

Due to insufficient mesh and/or time resolutions, the solutions of ρk and $\rho\varepsilon$ can exhibit negative values, especially in regions of strong stable stratification. Besides being unphysical,

such values will generate negative turbulence diffusivities for the transport equations, thus causing the numerical solution to diverge.

In order to avoid numerical instabilities, the following "clipping" procedures have been developed and implemented in the model. The procedures will readjust, if necessary, the nodal values of ρk and $\rho\varepsilon$ such that the resulting nodal values of eddy viscosity (K) are within a desired range $[K_{min}, K_{max}]$, which are input parameters of the model. The procedures consist of the following steps:

1. Search through the entire computational domain for the maximum values of ρk and $\rho\varepsilon$ and call them $(\rho k)_{max}$ and $(\rho\varepsilon)_{max}$.

2. Define the minimum values of ρk and $\rho\varepsilon$ to be

$$(\rho k)_{min} = 10^{-6}(\rho k)_{max} ,$$
$$(\rho\varepsilon)_{min} = 10^{-6}(\rho\varepsilon)_{max} .$$

3. For nodal points with $\rho k < (\rho k)_{min}$ or $\rho\varepsilon < (\rho\varepsilon)_{min}$, adjust their values to be

$$\rho k = (\rho k)_{min} ,$$
$$\rho\varepsilon = C_\mu (\rho k)^2_{min} / \rho \ K_{min} .$$

4. Evaluate nodal values of eddy viscosity (K) according to Eq. (4.27).

5. Readjust nodal values of ρk and $\rho\varepsilon$ so that the values of K are within the specified range $[K_{min}, K_{max}]$. Specifically, if $K < K_{min}$, set

$$K = K_{min} \text{ and } \rho k = \left(\rho K_{min} \cdot \rho\varepsilon / C_\mu\right)^{1/2} .$$

If $K > K_{max}$, set

$$K = K_{max} \text{ and } \rho\varepsilon = C_\mu (\rho k)^2 / \rho K_{max} .$$

After applying the above "clipping" procedures, boundary condition for $\rho\varepsilon$ is finally updated according to

$$\rho\varepsilon = \rho\left(C_\mu^{1/2} k\right)^{3/2} / \kappa\Delta \qquad (4.28)$$

for any nodes on the boundary over which the logarithmic wall function is used. In Eq. (4.28), κ is the Van Karman constant and Δ is the standoff distance between the boundary of the computational domain and the nearby solid surface. On the same boundary, the natural boundary condition of $\frac{\partial(\rho k)}{\partial n} = 0$ is applied for the k-equation. For the momentum equation in the streamwise direction, a momentum flux boundary condition in the following form is applied,

$$\rho K \frac{\partial u_t}{\partial n} = \rho (u_w - u_t) \left[\kappa \left(C_\mu^{1/4} k \right)^{1/2} \right] \Big/ \ell n \left[E \Delta \left(C_\mu^{1/4} k \right)^{1/2} / \upsilon \right] \tag{4.29}$$

in which u_w is velocity on the solid wall (usually zero), u_t is the streamwise velocity at the node under consideration, E is an empirical constant (9.0 for smooth wall), and υ is the dynamic viscosity. Similarly for the temperature equation, the following heat flux boundary condition is applied,

$$K^\theta \frac{\partial \theta}{\partial n} = (\theta_w - \theta) \left[\kappa \left(C_\mu^{1/4} k \right)^{1/2} \right] \Big/ \mathrm{Pr}\, t \ell n \left[E \Delta \left(C_\mu^{1/4} k \right)^{1/2} / \upsilon \right] \tag{4.30}$$

in which θ_w is temperature on the solid wall.

4.4 Numerical Examples

Before the final version of $k-\varepsilon$ turbulence submodel was applied to simulate the atmospheric dispersion of heavy gases, a standard version for isothermal flows was first implemented and assessed against results from two important laboratory experiments, namely, the fully developed channel flow of Laufer (1951) and the massively separated flow over a backward-facing step conducted by Kim (1978). In both cases, excellent agreement between the predicted results and measured data were observed. For brevity, results from these test problems are not included herein. In the following, two heavy-gas dispersion simulations, one for a laboratory test and the other for a field experiment, are presented and discussed. The two simulations have been performed using both the *K*-theory turbulence submodel and the more advanced $k-\varepsilon$ equation submodel, and the numerical predictions are compared with measured data to illustrate the improvements obtained with the advanced turbulence submodel.

4.4.1 Heavy-Gas Dispersion Simulation of a Wind Tunnel Experiment

This example is a simulation for one of the three laboratory experiments conducted by McQuaid (1976), which were designed to investigate the structure of shear flows with stable density stratification. The experiments were conducted in a wind tunnel with a fully developed rectangular channel flow of air into which carbon dioxide was introduced as a 'line' source at ground level. The simulated experiment, test No. 3, has the following test conditions: a source rate of 0.0227 kg/s, an average in-flow velocity of 1.28 m/s, and a source Richardson number (a measure of buoyancy versus turbulent flux) of 17.8.

The two-dimensional computational domain is defined by x=-0.82 m to 6.0 m and y=0 to 0.5 m, with the source centered at the origin of the coordinate system. A graded mesh consisting of 5,000 points (50 and 100 in the vertical and horizontal directions, respectively) was used in the calculation. The continuous source was modeled via injecting CO_2 , with a vertical injection velocity of 0.275 m/s, over a width of 0.08 m. At the inlet, a logarithmic velocity profile for a neutral atmospheric boundary layer, which is characterized by a friction velocity of 0.0528 m/s and a roughness length of 10^{-5} m, was assumed. The problem was simulated with both the similarity based *K*-theory and the $k-\varepsilon$ equation turbulence submodels. For the latter, a stand-off distance of 0.01 m above the ground surface was selected to permit the use of wall functions on such a boundary.

In Fig. 4.1, the predicted concentration contours obtained with the two turbulence submodels are depicted and compared. Overall a ground-hugging cloud is predicted by both submodels but the differences are quite noticeable, especially in the source region. Generally, the *K*-theory turbulence submodel predicts a somewhat higher cloud, together with significantly higher concentration in the source region. Such over-prediction of concentration is more clearly shown in Fig. 4.2 for the ground level concentrations. In contrary, the predictions by the $k-\varepsilon$ equation submodel are in much better agreement with the measured data, regarding both the concentration values and the slope of the curve in the downwind direction.

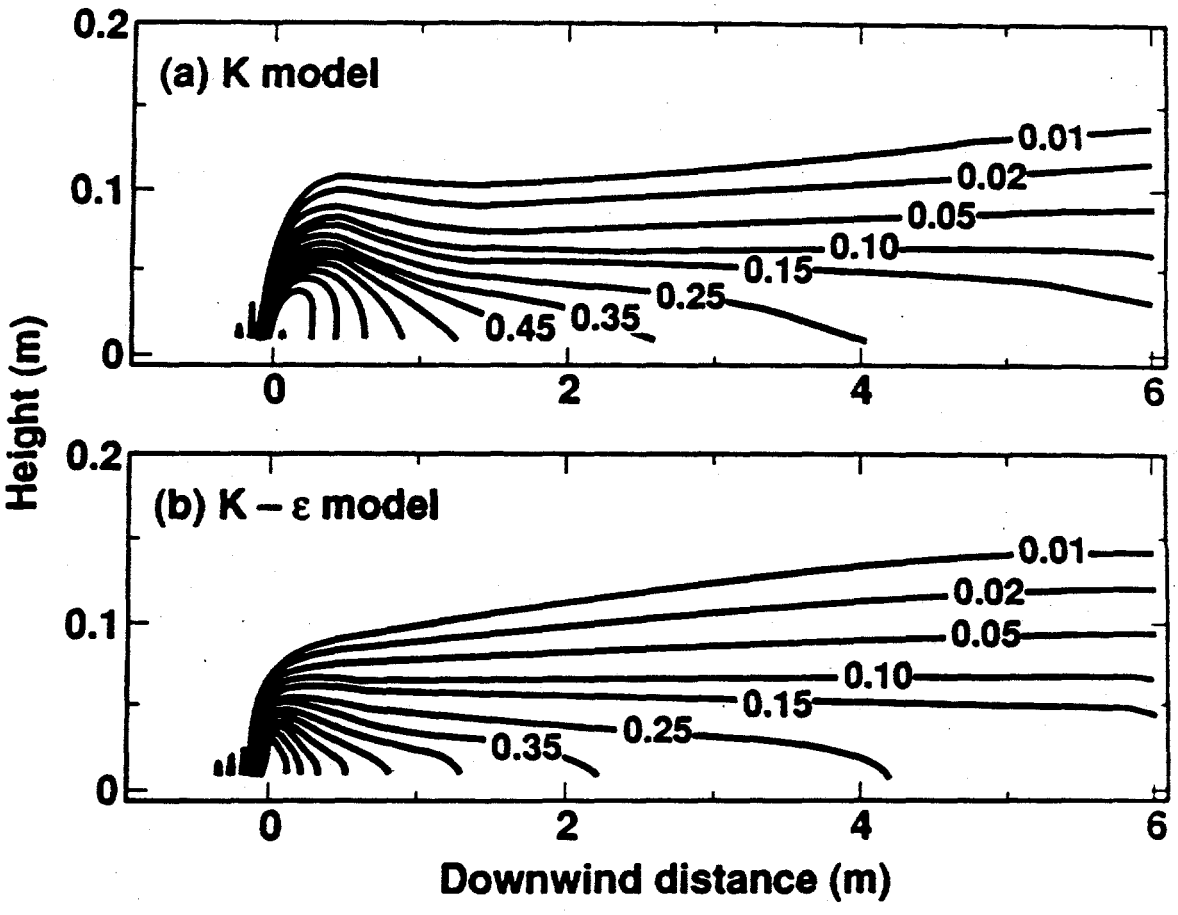

Fig. 4.1. Calculated concentration contours for McQuaid's experiment No. 3 by two turbulence models.

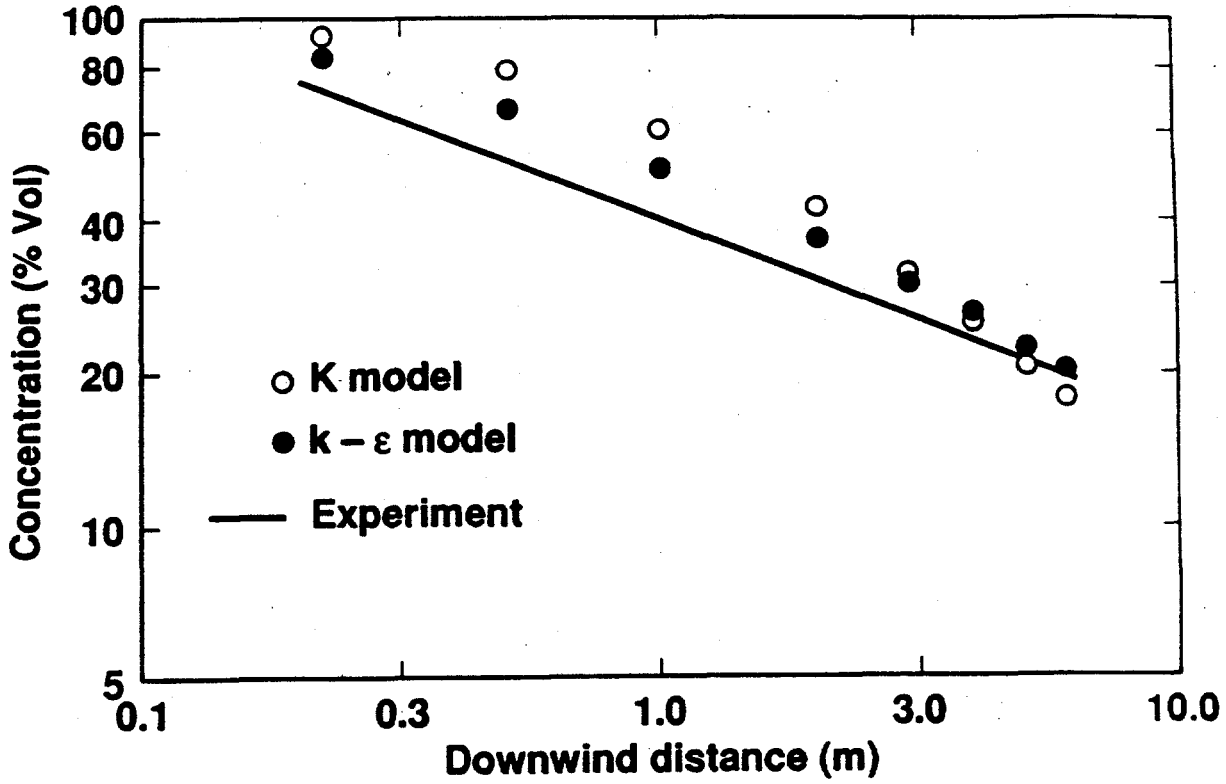

Fig. 4.2. Calculated versus measured ground level concentration for McQuaid's experiment No. 3.

Another important means to measure the accuracy of a turbulence submodel is its ability to predict concentration on the crosswind plane, in this case, the vertical direction (because of 2-D). This evaluation is especially important for a heavy gas cloud, because an inferior submodel may predict reasonably well the concentration in the downwind direction and yet with grossly inaccurate cloud shape, typically a narrower and higher cloud than reality. Such assessments are made in the next two figures. In Fig. 4.3, a comparison is made for the predicted heights corresponding to 50% ground level concentration for various downwind locations. Again, results from the $k-\varepsilon$ submodel are in much better agreement with the measured data than those obtained with the *K*-theory submodel, especially near the source. The improvement obtained with the $k-\varepsilon$ turbulence submodel is further illustrated in Fig. 4.4 for the concentration profile, i.e., concentration versus height, at x = 0.54 m behind the source.

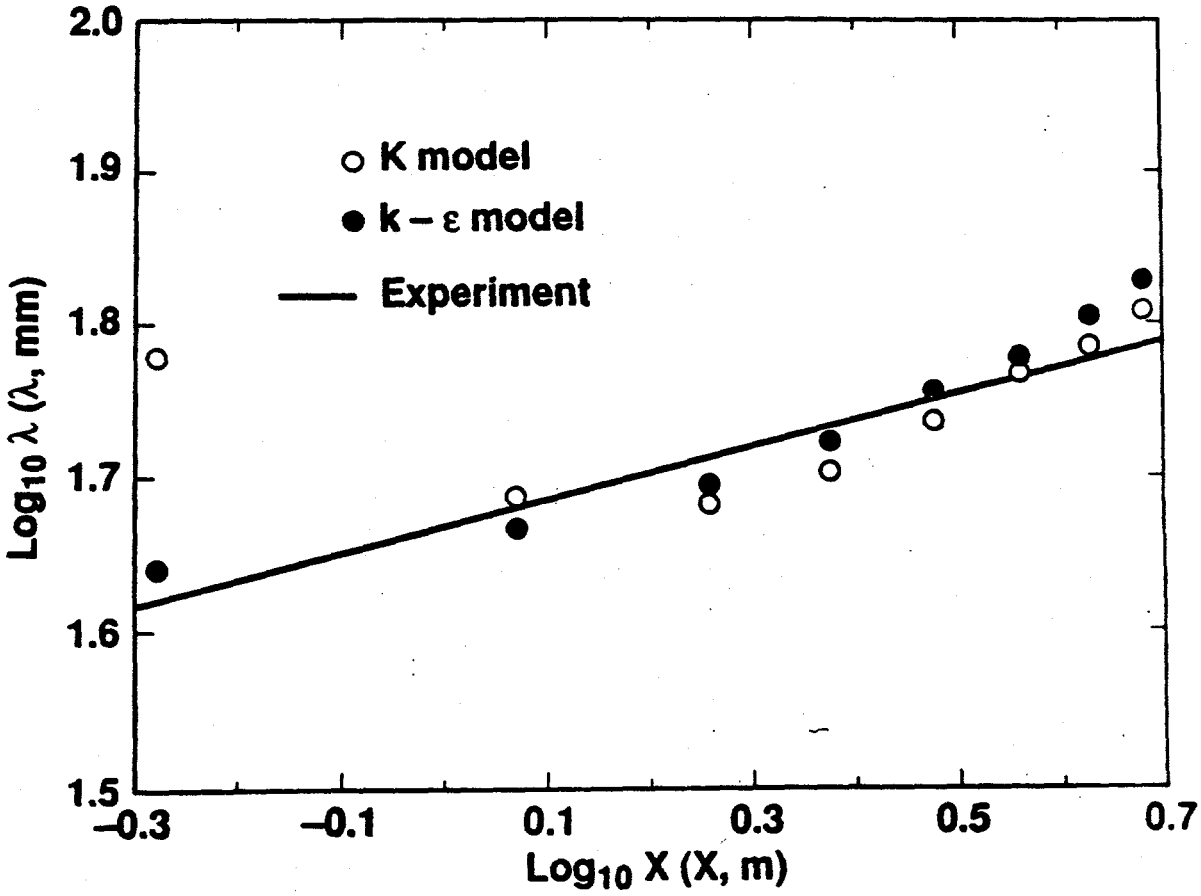

Fig. 4.3. Calculated versus measured values of λ (the height with 50% ground level concentration) for McQuaid's experiment No. 3.

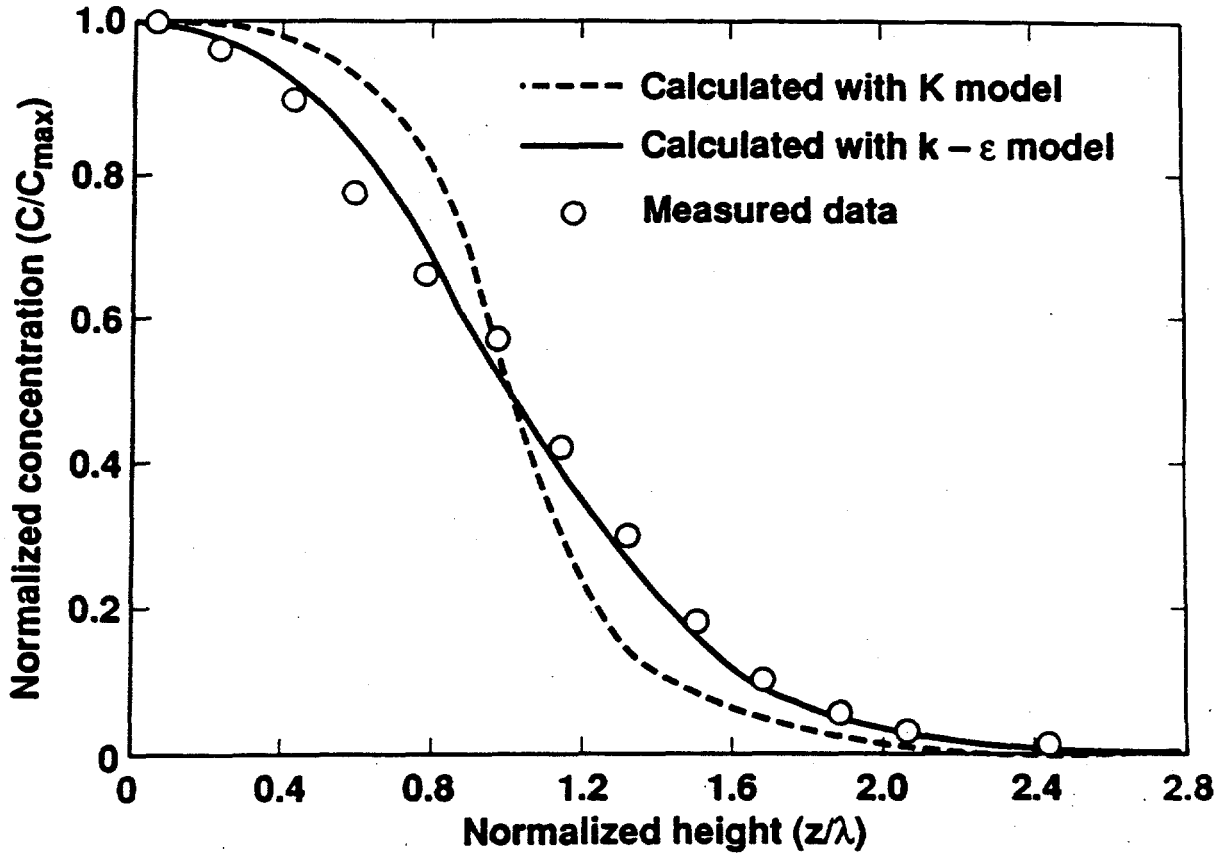

Fig. 4.4. Calculated versus measured concentration profiles at $x = 0.54m$ for McQuaid's experiment No. 3.

4.4.2 Vapor Dispersion Simulation of an LNG Spill

The following is a simulation for one of the LNG vapor dispersion experiments, named Burro series, conducted by LLNL in 1980 (Koopman, *et al.*, 1982). The experiment being simulated is Burro-8, which was conducted under very low wind speed and stable atmospheric conditions. During the test, 28 m^3 of LNG was piped onto the spill pond at a rate of 16 m^3/min. The atmospheric conditions were: an average wind speed of 1.8 m/s at 2-m height, an estimated friction velocity of 0.074 m/s, a Monin-Obukhov length scale of 16.5 m, and an adiabatic lapse rate of approximately -0.02°C/m. Again, the problem was simulated with the *K*-theory turbulence submodel and the $k-\varepsilon$ equation submodel.

In the numerical simulations, a logarithmic velocity profile based on measured data was assumed at the inlet plane and also used as initial conditions. Flat terrain is considered herein and the vapor cloud is assumed to be symmetric about the vertical plane bisecting the spill area and along the prevailing wind direction, thus allowing only one-half of the vapor cloud to be simulated. The computational domain has the following dimensions: 500 m longitudinally, 120 m laterally, and 15 m vertically. The total number of mesh points is 9,568 (46 x 16 x 13 in the above directions). The spilled LNG was modeled via injecting NG vapor over a source area of 25.6 m x 12.8 m (for one-half of the source) with a vertical injection velocity of 0.13 m/s over a period of 108 s. In both simulations, heat transfer between the ground surface and the vapor cloud was treated via a bulk heat transfer submodel with an effective heat transfer velocity of 0.0125 m/s. For the $k-\varepsilon$ turbulence submodel, the bottom boundary was defined at 0.05 m above the ground over which wall functions were applied for the momentum equations. Another simulation was also made with the $k-\varepsilon$ equation submodel, together with the turbulent heat transfer defined by Eq. (4.30), instead of the bulk heat transfer submodel. A somewhat higher and narrower vapor cloud was observed, suggesting an over-prediction of turbulent heat flux and the need of fine tuning Eq. (4.30) for LNG simulations. The large differences in temperature between the ground and vapor cloud are probably far beyond the range Eq. (4.30) was originally developed for.

In Figs. 4.5 and 4.6, some sample results obtained with the $k-\varepsilon$ turbulence submodel are depicted. Fig. 4.5 shows the predicted concentration contours and the velocity projection on a plane 1 m above the ground. Profound changes of the velocity field from the originally unidirectional wind field is apparent and the concentration contours manifest clearly the gravity spreading of the vapor cloud in all directions, including upwind. In addition, a bifurcated vapor cloud is seen, as suggested by those concentration levels higher than 15%. The lateral spread of the vapor cloud is further examined in Fig. 4.6. Due to the presence of density gradient in the lateral direction, an outward moving vortex is formed and air is entrained from the top surface into the vapor cloud, thus resulting in a "nose shape" region near the advancing front of the cloud.

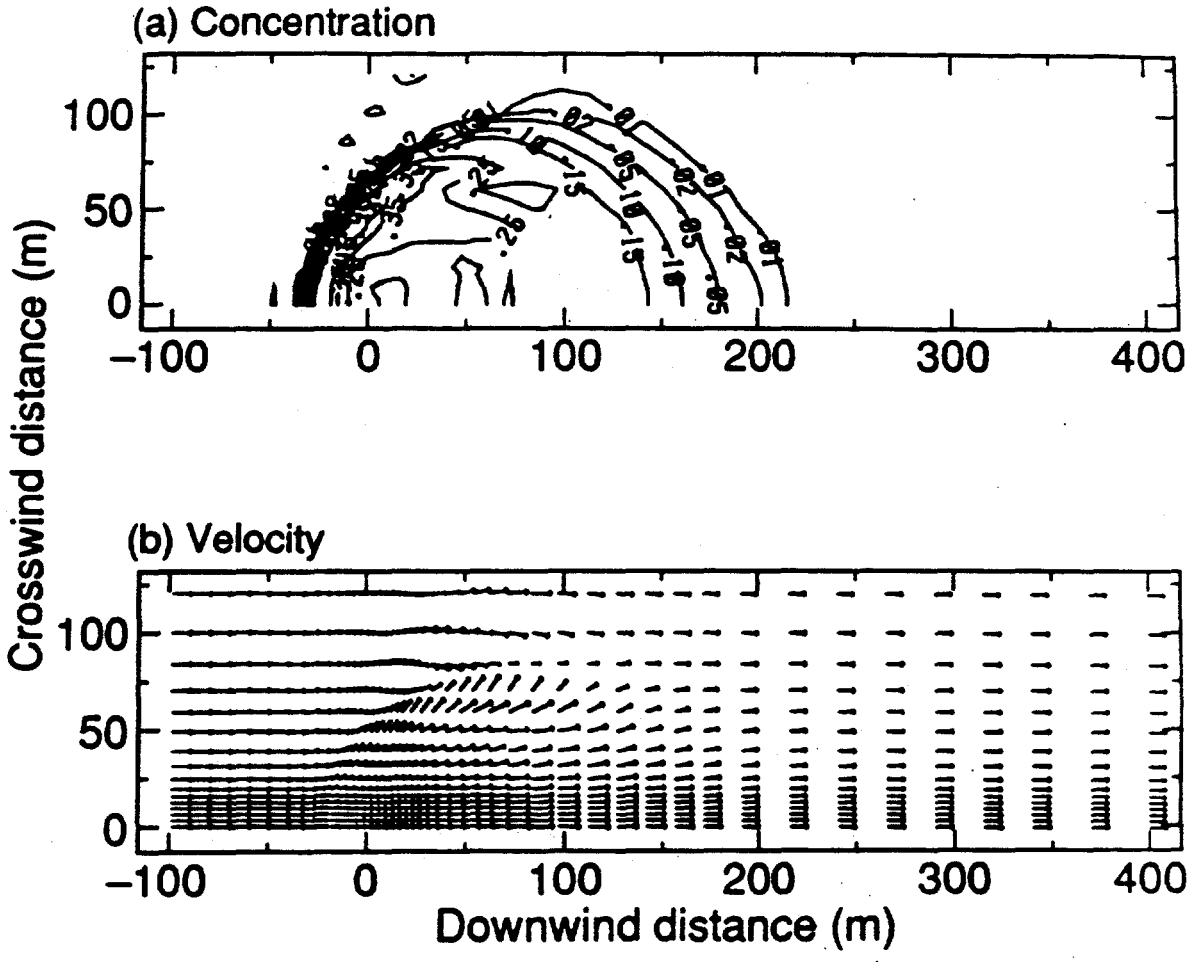

Fig. 4.5. **Burro 8 calculated concentration contours and velocity vectors on the horizontal plane 1 m above ground at $t = 120s$.**

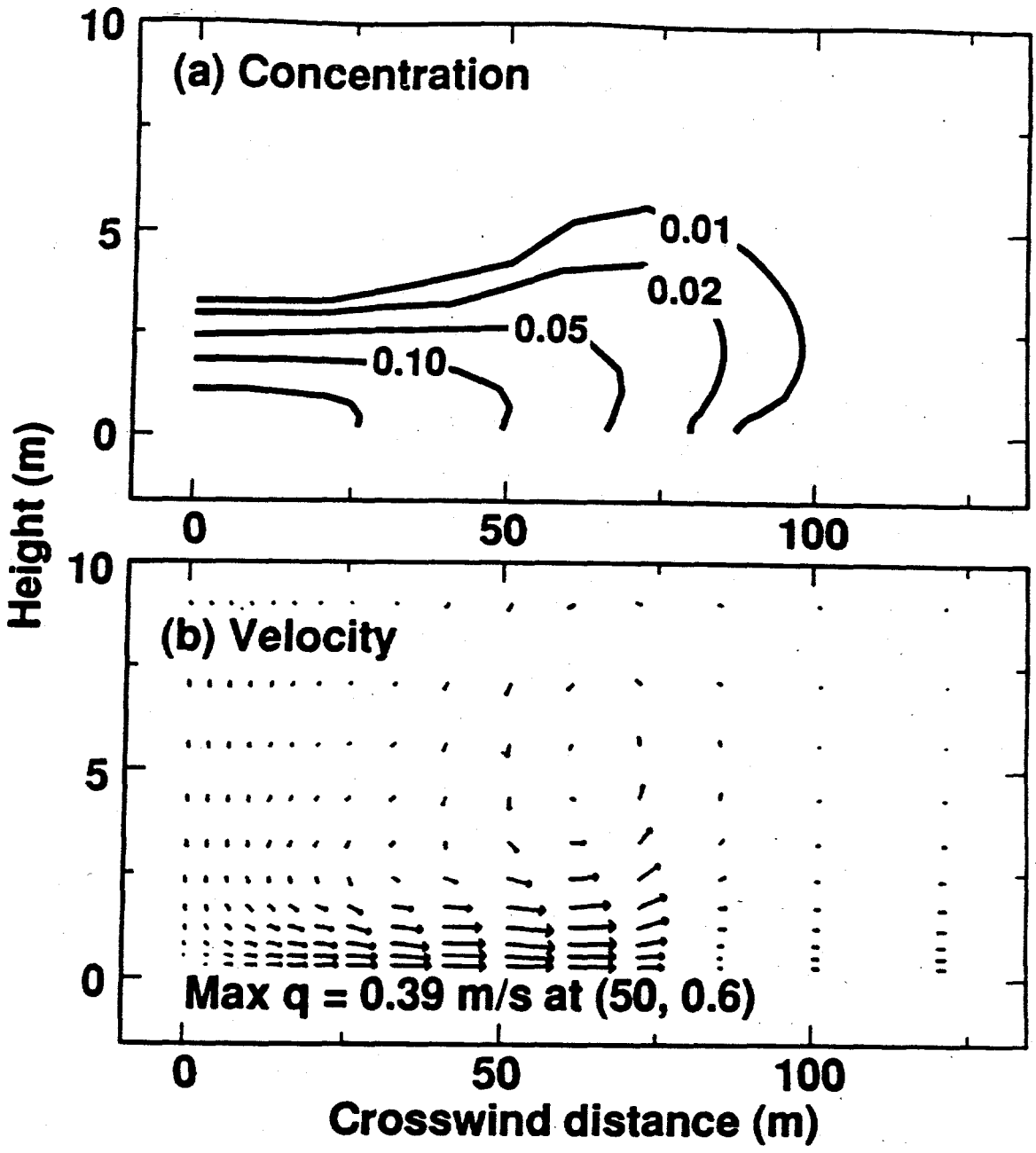

Fig. 4.6. **Burro 8** calculated concentration contours and velocity vectors on the crosswind plane 140 m downwind at $t = 120s$.

In Fig. 4.7, a comparison is made between the predicted and measured concentrations on the plane 1 m above ground at t = 120 s. Both turbulence submodels are seen to be able to predict gravity spread and the shape of the vapor cloud reasonably well. However, the wider cloud predicted by the $k-\varepsilon$ model is apparently in better agreement with the measured data, particularly, regarding features such as cloud shape and cloud bifurcation.

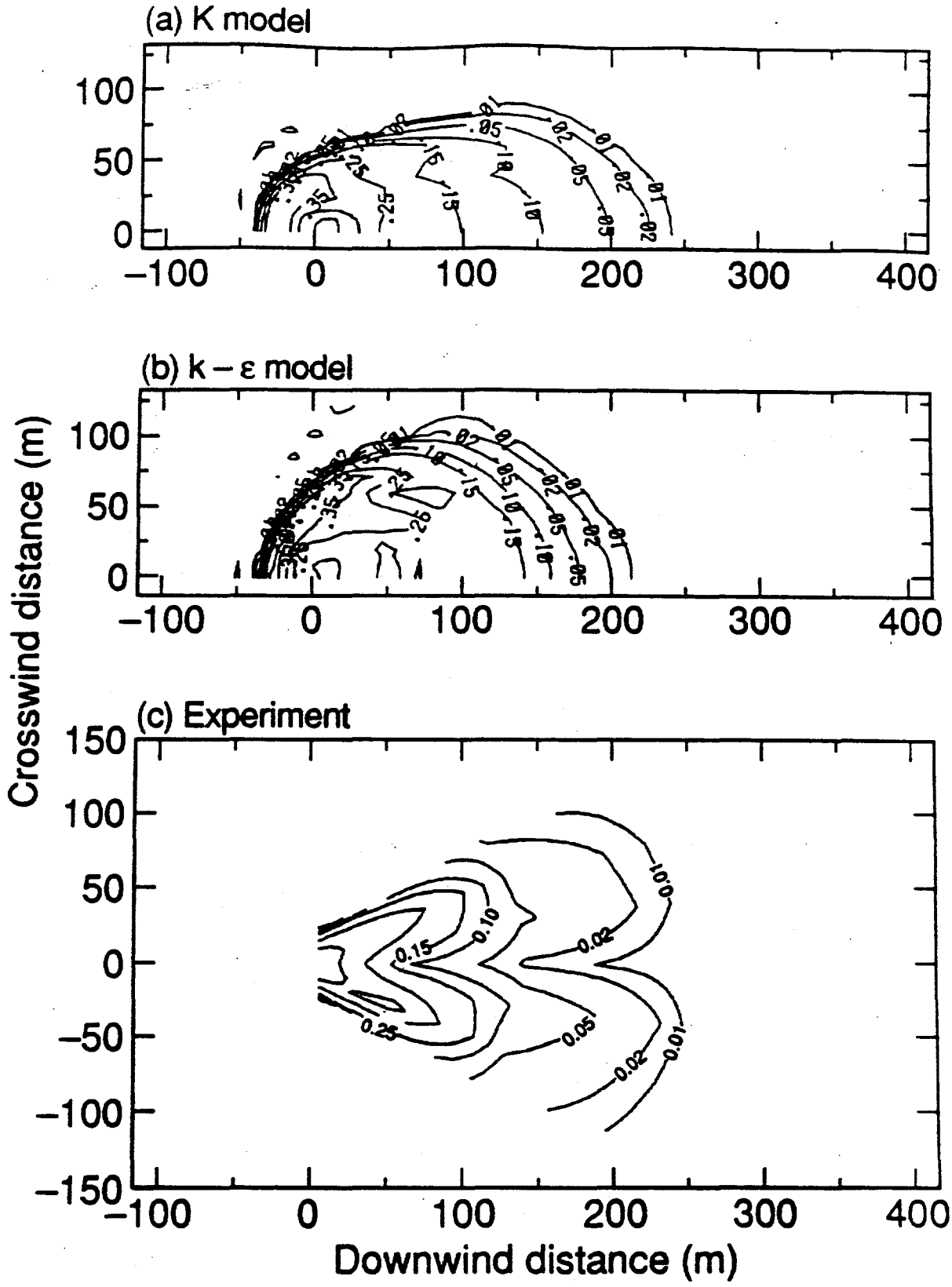

Fig. 4.7. Burro 8 calculated versus measured concentration contours on the horizontal plane 1 m above ground at $t = 120s$.

In Fig. 4.8, the corresponding concentration contours on a crosswind plane 140 m downwind are compared. Again, results from the $k-\varepsilon$ model are observed to agree much better with experimental data regarding the cloud height, its bifurcated structure, and the width as well. Unfortunately, the exact width of the cloud can not be determined because the cloud spread beyond the edges of the sensor array.

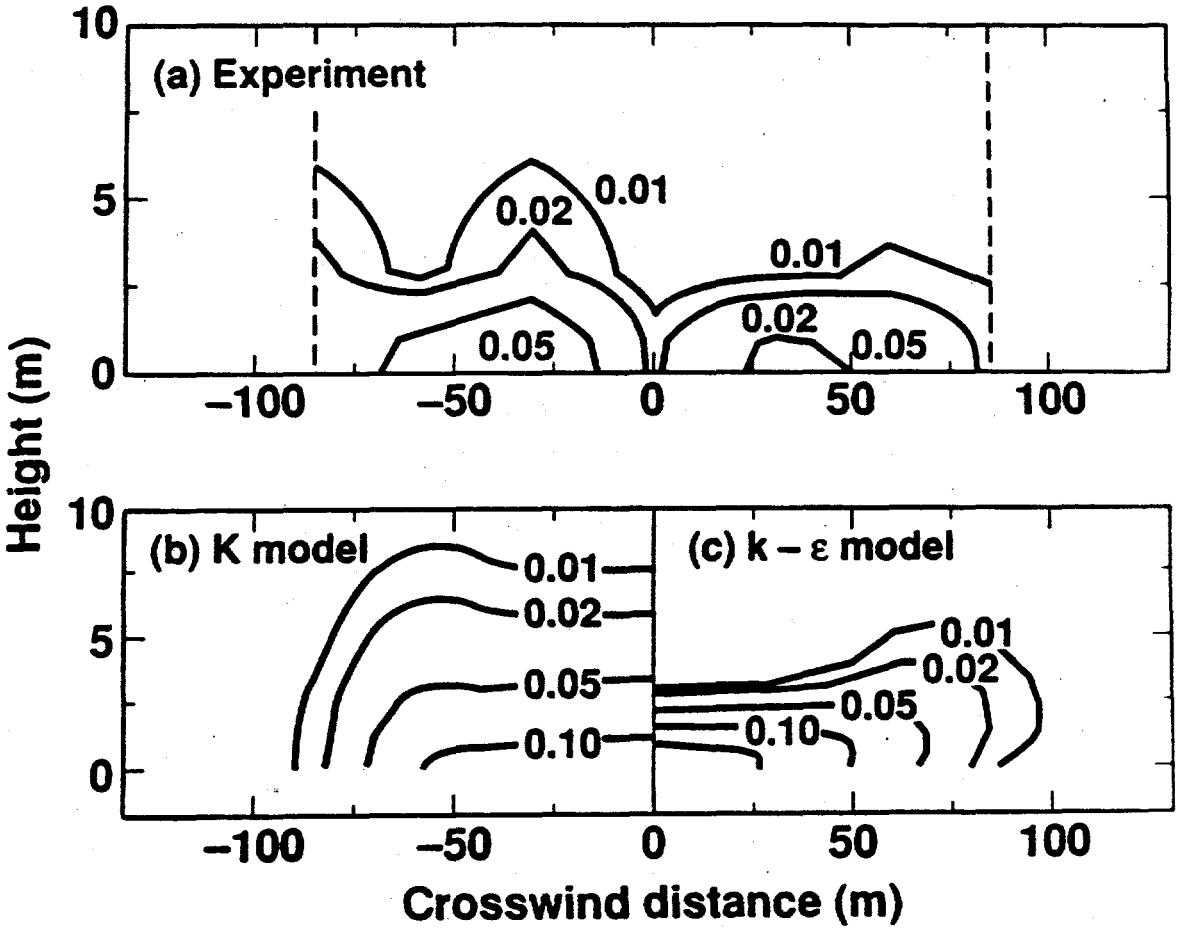

Fig. 4.8. Burro 8 calculated versus measured concentration contours on the crosswind plane 140 m downwind at $t = 120s$.

Finally, the predicted time histories of concentration and temperature for a selected location, at 57 m downwind and on the cloud centerline, are compared with field measurements in Figs. 4.9 and 4.10 respectively. Although both submodel appear to simulate the field data reasonably well, the improvements gained by the $k-\varepsilon$ submodel, typically 5% in (absolute) concentration value and 10°C in temperature, are quite significant. The larger discrepancies between numerical predictions by both submodels and the measured data for late times ($t > 160$ s) are believed partly due to the inadequacy of the ground heat transfer submodel, such as over-heating from the ground, and partly due to the meandering of the actual vapor cloud (which was indeed not treated in the numerical simulations).

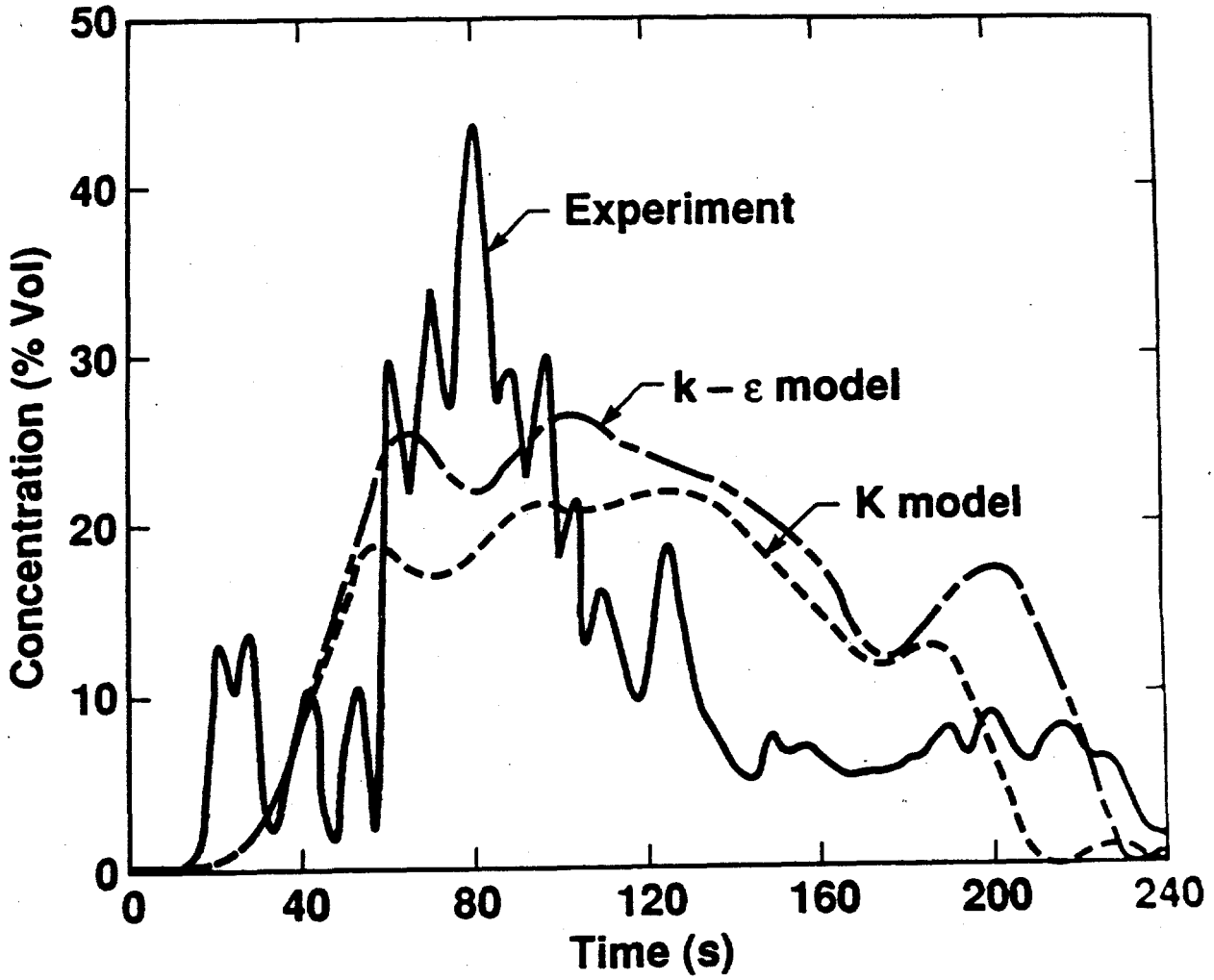

Fig. 4.9. Burro 8 calculated versus measured concentration for a point on the cloud centerline at 57 m downwind and 1 m above ground.

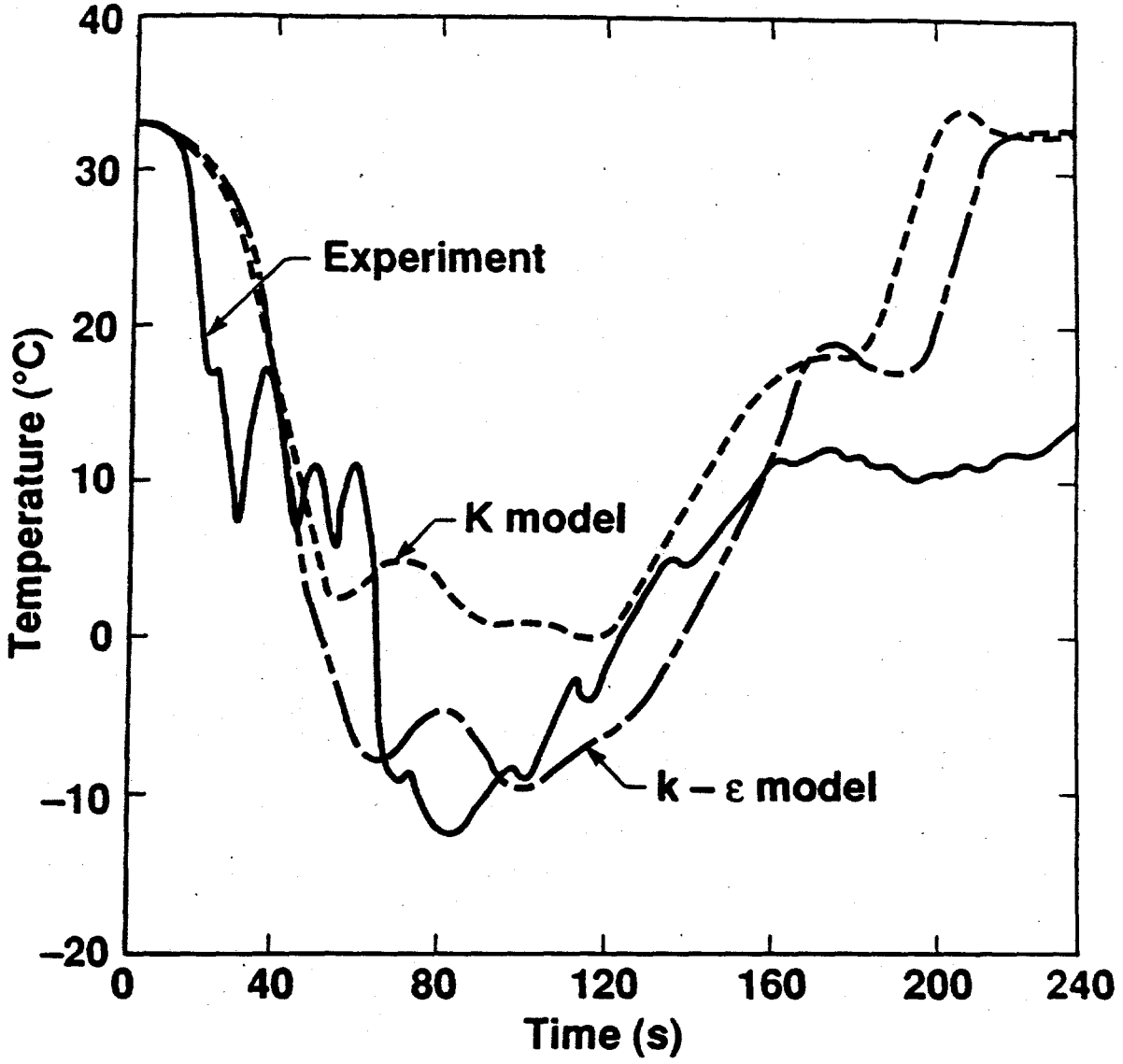

Fig. 4.10 Burro 8 calculated versus measured temperature for a point on the cloud centerline at 57 m downwind and 1 m above ground.

5. *CONCLUDING REMARKS*

In this study, two major improvements have been made to the FEM3A model: improved mass conservation for treating dispersion scenarios with large density changes, and the addition of an advanced turbulence submodel based on solving the $k-\varepsilon$ transport equations. These enhancements have resulted in substantial improvements in the dispersion simulations, as demonstrated by the numerical examples. Additionally, they have greatly extended the range of applicability of the model, including the ability to treat problems with density variations beyond the LNG range and dispersion scenarios of greater complexities, such as those involving significant flow separations and recirculations.

Results from the present study indicate that, for problems with density variations in the LNG range, the FEM3A model is adequately accurate. The results of this study also suggest that the new algorithm can be cost-effective in restoring the conservation properties for most heavy-gas dispersion involving large density variations. More specifically, when density variations are predominantly caused by high molecular weight and high concentration of the species (as opposed to large changes in temperature and/or dynamic pressure), solving the reformulated species equations alone is sufficient to conserve the species mass and, with reasonable accuracy, the global mass as well. The omission of the $\partial\rho/\partial t$ term in the global mass conservation equation appears to have only little effect on global mass conservation and can probably be tolerated for most applications. This is important and fortunate, because the inventory of global mass for most heavy-gas dispersion problems is often time-dependent and inconvenient to determine.

For problems wherein large density variations are primarily caused by temperature differences, enforcing species conservation alone may no longer lead to adequate conservation of global mass. In such cases, global mass conservation may become equally important and should also be enforced. Further investigation and development are necessary in order to adequately address such cases. Similar type of problems in a closed domain have been considered by Chenoweth and Paolucci (1986).

Although the algebraic K-theory turbulence submodel in FEM3A has performed reasonably well in the past for a relatively wide range of heavy-gas dispersion simulations, it is based on similarity theory and is thus strictly valid only for situations wherein the flow is predominantly the boundary-layer type. In contrary, more complete physics are treated in the $k-\varepsilon$ equation turbulence submodel, including transport effects and more realistic length scales. As a result, significantly improved predictions over the K-theory submodel have been observed. Such a turbulence submodel can greatly extend the code's ability in dealing with dispersion scenarios of greater complexities, including flows with significant separation and recirculation.

While the $k-\varepsilon$ turbulence submodel has been shown to yield substantially improved predictions over the K-theory submodel, its major shortcoming is probably the uncertainty associated with the use of wall functions. If not used properly, the quality of the numerical solution could be severely contaminated. To assure the quality of the numerical solution, care must be exercised to make sure that the standoff distance (Δ) between the computational boundary and the solid wall is selected properly so that the wall laws are valid on the computational boundary. As a check on the validity of Δ, one should make sure the value of

$u_* \Delta/\upsilon$ (in which u_* is the friction velocity, $u_* = (0.3k)^{\frac{1}{2}}$, and υ is the molecular viscosity of the fluid) on the boundary as given by the numerical solution is between 30 and 200. There are advanced turbulence submodels that permit the governing equations to be integrated all the way to the wall, thus eliminating the need of using wall functions. These include the $k-\omega$ equation model of Wilcox (1988) and the second-moment closure (7-equation) model developed by Launder and Shima (1989). LLNL has some experience (and with encouraging results) in using the $k-\omega$ model and is in the process of implementing the Launder-Shima turbulence model into a new incompressible Navier-Stokes code. These turbulence submodels, as expected, are computationally more expensive; however, with some further developments, their utility for heavy-gas dispersion simulations is feasible in the near future.

Regarding computer time, the additional computing cost associated with the reformulated equations to enforce mass conservation is nominal, while the upgrading of turbulence modeling from the algebraic K-theory to the $k-\epsilon$ transport equations is more substantial. Our numerical experiments for a few medium-size problems employing a direct solver, in conjunction with subcycling to effectively solve the pressure equation, indicate an increase of 40-60% in CPU cost. However, for large problems that the matrix of the pressure equation can no longer fit the available computer memory, the cost associated with solving the pressure equation is expected to be much higher and thus the percentage increase in CPU time using the $k-\epsilon$ turbulence submodel should be smaller.

6. *REFERENCES*

Betts, P.L., and V. Haroutunian, 1988: Finite Element Calculations of Transient Dense Gas Dispersion. "Stably Stratified Flow and Dense Gas Dispersion", Edited by J.S. Puttock, Clarendon Press, pp. 349–384.

Blewitt, D.M., J.F. Yohn, R.P. Koopman, and T.C. Brown, 1987: Conduct of Anhydrous Hydrofluoric Acid Spill Experiments. *Proc. of the International Conference on Vapor Cloud Modeling*, New York, NY, pp. 1–38.

Chan, S.T., 1983: FEM3—A Finite Element Model for the Simulation of Heavy-Gas Dispersion and Incompressible Flow: User's Manual. UCRL-53397, Lawrence Livermore National Laboratory, Livermore, CA.

Chan, S.T., 1988: FEM3A—A Finite Element Model for the Simulation of Gas Transport and Dispersion: User's Manual. UCRL-21043, Lawrence Livermore National Laboratory, Livermore, CA.

Chan, S.T., 1992: Numerical Simulations of LNG Vapor Dispersion from a Fenced Storage Area. *Journal of Hazardous Materials*, **30**, pp. 195–224.

Chan, S.T., 1994: FEM3C—An Improved Three-Dimensional Heavy-Gas Dispersion Model: User's Manual. UCRL-MA-116567, Rev. 1, Lawrence Livermore National Laboratory, Livermore, CA.

Chan, S.T., D.L. Ermak, and L.K. Morris, 1987a: FEM3 Model Simulations of Selected Thorney Island Phase I Trials. *Journal of Hazardous Materials*, **16**, pp. 267–292.

Chan, S.T., H.C. Rodean, and D.N. Blewitt, 1987b: FEM3 Modeling of Ammonia and Hydrofluoric Acid Dispersion. *Proc. of the International Conference on Vapor Cloud Modeling*, American Institute of Chemical Engineers, New York, NY, pp. 116–154.

Chan, S.T., H.C. Rodean, and D.L. Ermak, 1984: Numerical Simulations of Atmospheric Release of Heavy Gases over Variable Terrain. Air Pollution Modeling and Its Application III, Plenum Press, pp. 295–341.

Chenoweth, D.R., and Paolucci, 1986: Natural Convection in an Enclosed Vertical Air Layer with Large Horizontal Temperature Difference. *Journal of Fluid Mechanics*, **169**, pp. 173–210.

Dyer, A.J., 1974: A Review of Flux-Profile Relationships. *Boundary-Layer Meteor.*, 7, 363–372.

Engelman, M.S., R.L. Sani, and P.M. Gresho, 1982: The Implementation of Normal and/or Tangential Boundary Conditions in Finite Element Codes for Incompressible Fluid Flow. *Int. J. Num. Meth. Fluids*, **2**, 225–238.

Ermak, D.L., and S.T. Chan, 1985. A Study of Heavy Gas Effects on the Atmospheric Dispersion of Dense Gases. *Air Pollution Modeling and Its Application V*, Plenum Press, pp. 723–742.

Ermak, D.L., and S.T. Chan, 1986: Recent Development on the FEM3 and SLAB Atmospheric Dispersion Models. *Proceedings of the IMA Conference on Stably Stratified Flows and Dense-Gas Dispersion*, Clarendon Press, Oxford, 261–283.

Ermak, D.L., S.T. Chan, D.L. Morgan, and L.K. Morris, 1982. A Comparison of Dense-Gas Dispersion Model Simulations with Burro Series LNG Spill Test Results. *Journal of Hazardous Materials*, **6**, pp. 129–160.

Gresho, P.M., Chan, S.T., Upson, C.D., and Lee, R.L., 1984. A Modified Finite Element Method for Solving the Time-Dependent, Incompressible Navier-stokes Equations: Part 1—Theory; Part 2—Application. *International Journal for Numerical Methods in Fluids*, **4**, pp. 557–598 and 619–640.

Haroutunian, V., 1987: A Time-Dependent Finite Element Model for Atmospheric Dispersion of Gases Heavier than Air. Ph.D. Dissertation, The University of Manchester Institute of Science and Technology, United Kingdom.

Havens, J.A., T.O. Spicer, and P.J. Schreurs, 1987: Evaluation of 3-Dimensional Numerical Models for Atmospheric Dispersion of LNG Vapor. *Proceedings of the International Conference on Vapor Cloud Modeling*, American Institute of Chemical Engineers, New York, 495–538.

Kim, J.J., 1978: Investigation of Separation and Reattachment of a Turbulent Shear Layer: Flow over a Backward-Facing Step. Ph.D. Thesis, Stanford University, CA.

Koopman, R.P., R.T. Cederwall, D.L. Ermak, H.C. Goldwire, Jr., W.J. Hogan, J.W. McClure, T.G. McRae, D.L. Morgan, H.C. Rodean, and J.H. Shinn, 1982: Analysis of Burro Series $40-m^3$ LNG Spill Experiments. *J. Haz. Materials*, **6**, 43–83.

Laufer, J., 1951: Investigation of Turbulent Flow in a Two-Dimensional Channel. NACA Report No. 1053.

Launder, B.E., 1984: Second-Moment Closure: Methodology and Practice. *Turbulence Models and Their Applications*, **2**, Eyrolles.

Launder, B.E., and N. Shima, 1989: Second-Moment Closure for the Near-Wall Sublayer: Development and Application. *AIAA Journal*, 27, pp. 1319–1325.

Launder, B.E., and D.B. Spalding, 1974: The Numerical Computation of Turbulent Flows. *Computer Methods in Applied Mechanics and Engineering*, **3**, pp. 269–289.

Lee, R.L., P.M. Gresho, S.T. Chan, and C.D. Upson, 1983: A Three-Dimensional, Finite Element Model for Simulating Heavier-than-Air Gaseous Releases over Variable Terrain. Air Pollution Modeling and Its Application II, Plenum Press, pp. 555–573.

Leone, Jr., J.M., H.C. Rodean and S.T. Chan, 1985: FEM3 Phase-Change Model. UCID-20353, Lawrence Livermore National Laboratory, Livermore, CA.

McQuaid, J., 1976: Some Experiments on the Structure of Stably Stratified Shear Flows. Technical Paper P21, *Safety in Mines Research Establishment*, Sheffield, U.K.

Ogura, Y., and N. Phillips, 1962: Scale Analysis of Deep and Shallow Convection in the Atmosphere. *Journal of Atmospheric Sciences*, **19**, pp. 173–179.

Rodean, H.C., 1987a: FEM3 Simulations of Vapor Dispersion From a Random Pattern of Munitions. UCRL-53790, Lawrence Livermore National Laboratory, Livermore, CA.

Rodean, H.C., 1987b: Mass Conservation for Instantaneous Sources in FEM3 Simulations of Material Dispersion. UCID-21226, Lawrence Livermore National Laboratory, Livermore, CA.

Rodi, W., 1980: Turbulence Models and Their Application in Hydraulics. International Association for Hydraulics Research, Delft, The Netherlands.

Schotte, W., 1987: Fog Formation of Hydrogen Fluoride in Air. *Ind. Eng. Chem. Res.*, **26**, pp. 300–306.

Ueda, H., S. Mitsumoto, and S. Komori, 1981: Buoyancy Effects on the Turbulent Transport Processes in the Lower Atmosphere. *Quart J.R. Met. Soc.*, **107**, pp. 561–578.

Wilcox, D.C., 1988: Reassessment of the Scale-Determining Equation for Advanced Turbulence Models. *AIAA Journal*, 26, pp. 1299–1310.

ACKNOWLEDGMENTS

This work was performed under the auspices of the U.S. Department of Energy by the Lawrence Livermore National Laboratory (LLNL) under Contract No. W-7405-Eng-48. Funding for this study was provided by the U.S. Army Edgewood Research, Development and Engineering Center (ERDEC), Arberdeen Proving Ground, Maryland under MIPRs 1131-1532, 3311-1481 and 4311-1591. Ray Jablonski and Ron Pennsyle were the ERDEC scientific advisers. The author would like to thank Philip Gresho and Howard Rodean of LLNL for their contributions to improving the mass conservation properties of the new model. Lourdes Placeres patiently and skillfully typed the manuscript.